Corrosion Science xxx (xxxx) 111265

Contents lists available at ScienceDirect

Corrosion Science

journal homepage: www.elsevier.com/locate/corsci

# Corrosion of austenitic stainless steel at 90 °C under highly saline and anoxic conditions: A microspectroscopic study

Nicolas Finck [a, 1, *], Nikoleta Morelová [a, 2], Michel L. Schlegel [b, 3], Dieter Schild [a, 4], Solenn Reguer [c, 5], Kathy Dardenne [a, 6], Horst Geckeis [a, 7]

[a] Institute for Nuclear Waste Disposal (INE), Karlsruhe Institute of Technology (KIT), Hermann-von-Helmholtz-Platz 1, 76344 Eggenstein-Leopoldshafen, Germany
[b] Université Paris Saclay, CEA, Service de Recherche en Matériaux et Procédés Avancés, 91191 Gif-sur-Yvette, France
[c] DiffAbs Beamline, Synchrotron SOLEIL, L'Orme des Merisiers, Départementale 128, 91190 Saint-Aubin, France

ARTICLE INFO

*Keywords:*
Stainless steel (A)
AFS (B)
SEM (B)
XRD (B)
XPS (B)

ABSTRACT

The stainless steel AISI 309 S used for containers for vitrified high-level radioactive waste was exposed to 90 °C under highly saline and anoxic conditions for different exposure times up to 294 days. The surface damage was limited and no pitting could be detected. The corrosion layer is made of an inner-layer mostly of chromium (hydr)oxides and an outer-layer made of Fe- and Ni-based spinel compounds with admixed nickel (hydr)oxides. Minor contributions of magnetite and layered double hydroxide could be identified. Dissolved amounts of metal ions were very low, the pH increased only slightly and the redox potential decrease was limited.

## 1. Introduction

Operation of nuclear power plants generates significant amounts of high-level radioactive waste (HLRW), which needs to be disposed of in a safe way to shield future generations from its possible harmful impact. Over time, it has been accepted that the safe management of this waste relies on disposal in stable deep underground geological formations [1, 2]. In such a repository hosted in crystalline, clay or salt rock, the waste is foreseen to be surrounded by successive engineered and geological barriers. In order to optimize the performance of repositories, materials are being selected for their mechanical and chemical properties. Indeed, the selected materials have to ensure that emplaced waste packages are retrievable or can be recovered in the repository post-closure period (reversibility). Over long term, they have to prevent porewater from contacting the waste matrix under the conditions of local heating due to radioactive decay (thermal phase). Consequently, detailed information on the corrosion behavior of materials under the specific repository-relevant conditions (e.g., water saturated, anoxic, elevated temperature) is required.

Rock salt is a possible geological formation for hosting a nuclear waste repository. In this case, the host rock bears the main safety function due to its viscoplastic properties closing fractures, cracks and pores. According to the German concept for instance, HLRW containers have to keep their integrity to guarantee the possible waste recovery for 500 years [3]. The assessment of the evolution of the repository near field in the unexpected case of solution access to the emplacement caverns requires knowledge on possibly forming corrosion phases and the interaction of released radionuclides with those secondary phases. Note as well that saline groundwaters are also expected in some clay rock formations being discussed as potential host rocks for HLRW such as the Jurassic and Lower-Cretaceous clay rock in Northern Germany [4] and sedimentary layers in Canada [5]. It appears thus necessary to study the corrosion behavior of candidate canister materials in highly saline solutions.

* Corresponding author.
*E-mail address:* nicolas.finck@kit.edu (N. Finck).
[1] 0000-0002-1940-4051
[2] 0000-0002-7448-9107
[3] 0000-0002-8704-5038
[4] 0000-0001-6034-8146
[5] 0000-0002-7449-0503
[6] 0000-0003-1286-1855
[7] 0000-0002-0030-6697

https://doi.org/10.1016/j.corsci.2023.111265
Received 22 February 2023; Received in revised form 24 April 2023; Accepted 12 May 2023
0010-938/

Canisters containing vitrified nuclear waste must be made of material able to withstand constraints imposed by pouring the glass melt. The austenitic stainless steel AISI 309 S contains significant amounts of alloying elements such as Cr (22–24%) and Ni (12–14%) [6], making this material suited to construct canisters meeting these requirements. Stainless steel canisters filled with vitrified waste are usually proposed to be emplaced in an overpack, i.e., a thick walled carbon steel container, prior to disposal in an underground repository [7]. Depending on the disposal concept, the overpack acts as a corrosion buffer and needs to corrode first before water access to stainless steel canisters takes place. In the Swiss concept for instance, failure of the carbon steel container is assumed to occur after several thousands of years [8]. Within this study the corrosion of the inner stainless steel material was investigated with a focus on the forming corrosion phases.

Austenitic stainless steel is classified as corrosion-resistant material due to the formation of a passivating protective film on the surface, which considerably reduces the rate of general corrosion [7]. However, localized attack can take place on passivated surfaces causing the formation of pits under the influence of aggressive anions such as halides (e.g., $Cl^-$) [9,10]. The mechanism of pit initiation and growth are relatively well understood (e.g., [9]), and chloride anions play an important role in these processes. In the groundwater of most geological formations under consideration internationally, chloride is the dominant anion [11] with concentrations ranging from ~1450 mg/L in Callovo-Oxfordian [12] and ~10,200 mg/L in Opalinus Clay [13] to over hundred thousand mg/L for salt rock and some sedimentary rocks [11, 14–17]. Chloride anions are also present in significant amounts in the groundwater of crystalline host rock, such as in Sweden (in the range 2000 to 6000 mg/L in fractures at depths greater than 200 m at the Forsmark site [18]) or in Finland (brackish groundwater with salinity up to 10,000 mg/L dominates at depths between 30 and 400 m in the crystalline bedrock at Olkiluoto [19]). Groundwaters also typically contain other anions such as carbonate or sulfate, which reduce the tendency to pitting [9,10,20]. In addition, the susceptibility to localized corrosion in the presence of $Cl^-$ anions significantly decreases with increasing pH [11,21]. On the other hand, the tendency to pitting increases with temperature during the thermal phase [22]. Such a scenario, however, is only to be considered in case of unexpected early container failure. The best approach to identify the nature of forming corrosion products and to evaluate the corrosion behavior of specific canister materials is certainly to perform long-term in situ experiments under undisturbed conditions. Indeed, several studies have tested the in situ corrosion behavior of selected candidate canister materials under specific disposal conditions in underground research laboratories (e.g., [23–26]).

Over the past decades, several in situ corrosion experiments with stainless steel have been performed and outcomes have been reported [21,27–30]. Under anoxic and variable temperature conditions, the surface attack of AISI 316 L in contact with Opalinus Clay minerals was limited [30]. After 2 years at ambient temperature followed by 5 years at 85 °C, the observed corrosion damage was < 5 μm deep, with iron sulfides forming near to the original interface, Ni accumulating in the clay matrix close to the interface but almost no Cr was present adjacent to the steel. Similarly, no evidence of significant macroscopic corrosion could be detected at the surface of AISI 316 L or AISI 309 S in contact with Tournemire argillite for six years at ambient temperature [28,29]. Studies showed that both materials are resistant to corrosion under the applied conditions, which can be attributed to the ability of Cr to inhibit general corrosion in carbonate systems. Very low rates of general corrosion have also been reported for stainless steels of various grades corroding in direct contact with Boom Clay [21]. Interestingly, the welded material was not found more susceptible to corrosion than the parent material and the presence of a γ-radiation field had no observable effect on the measured uniform corrosion rates. Experiments have also been performed under in situ conditions in a former salt mine in Germany [21,27]. Both after 10 years at 90 °C or after 5.3 years at 190 °C, the extent of general corrosion of AISI 309 S was comparable (< 0.7 μm/a) to that obtained in contact with argillite [28–30]. However, in contact with salt rock the material suffered from pitting corrosion (maximum pit depth of 50 μm at 90 °C and 200 μm at 190 °C) and stress corrosion cracking (in the experiment at 190 °C). Unfortunately, no detailed structural characterization of the formed secondary products (i.e., corrosion phases) on the corroded specimens has been reported for these in situ experiments performed in salt rock.

The extent of general corrosion of stainless steels under the anoxic and elevated temperature conditions expected to prevail in rock salt repository has been reported in the literature, as detailed above, but no detailed structural investigations aiming to identify the nature of the secondary phases forming at the steel/brine interface has been reported so far. Stainless steel is an alloy made of several elements exhibiting different reactivity when exposed to specific conditions. A passivation layer typically develops at the surface of such materials, but is unlikely to contain only one element. Detailed analyses with modern analytical techniques are thus required to identify the exact nature of the formed secondary products and their chemical compositions. Owing to its inherent surface sensitivity, X-ray photoelectron spectroscopy is typically applied to analyze the layer forming on the steel surface, but is not adapted to probe the entire layer thickness. This limitation can be overcome by preparing samples as cross-sections and using techniques with high spatial resolution. This approach allows avoiding interferences from the underlying bulk material when probing the composition of the corrosion layer as a function of depth. This strategy has been applied successfully to analyze steel specimens exposed to argillite (e.g. [30]) but not to highly saline brines so far. Finally, the amounts of dissolved metal ions in the brine also depend on the solubility of the exposed corrosion products. Information on the composition of the contacting brine, including pH and redox potential, add further constrains on the nature of the underlying corrosion processes. The identification of the formed corrosion products and their formation mechanism will improve the general understanding of the corrosion behavior of stainless steel under the applied conditions. In addition, knowing the nature of the formed secondary phases will allow better evaluating the fate of radionuclides in a repository near-field in case of unexpected canister failure by performing uptake experiments with relevant corrosion products, and thus improve the Safety Case.

The corrosion behavior of the AISI 309 S stainless steel (thereafter abbreviated as 309 S) in concentrated sodium chloride or magnesium chloride solutions under anoxic and elevated temperature conditions has been investigated in this study (disposal concepts in rock salt). Polished coupons were suspended in brines in closed vessels in an anoxic glove box. After various contact times, vessels were opened and both the coupons and the brine were analyzed. pH and redox potential in the contacting brine were measured and detailed information on corrosion products was obtained from microscopic characterizations. Specifically, synchrotron-based micro X-ray fluorescence, micro X-ray diffraction and micro X-ray absorption spectroscopic analysis of the sample cross-section proved powerful at identifying the nature of the formed secondary phase(s) in order to formulate corrosion mechanism hypotheses.

## 2. Materials and methods

### 2.1. Materials and experimental setup

Coupons of 309 S (Table 1) were cut from a plate of 4 mm thickness using a water jet cutting machine to avoid the formation of heat-affected zones at edges and corners. Prior to use in corrosion experiments, all sides of the coupons were grinded with 500 SiC paper and subsequently polished with diamond containing paste up to a roughness of 0.25 μm. After polishing, coupons were cleaned with ethanol in

**Table 1**
Chemical composition (wt%) of used AISI 309 S steel (certificate EN 10204/3.1).

| C | Mn | Si | Cr | Ni | Mo | Cu | Fe |
|---|---|---|---|---|---|---|---|
| 0.06 | 1.15 | 0.35 | 22.45 | 13.17 | 0.23 | 0.23 | Balance |

an ultrasonic bath, dried and weighed before being placed in the Ar-filled box (< 1ppmv $O_2$) to avoid contact with oxygen.

Two 309 S coupons were suspended in each reactor using a PTFE (polytetrafluoroethylene) stand so that they did neither touch each other nor the inner wall of the reactor. Dimensions of the coupons were 18 mm × 10 mm × 4 mm and 14 mm × 8 mm × 4 mm. Reactors are made of a stainless steel body and a tantalum (a highly corrosion resistant material) inner liner and inner lid, and the tightness was ensured by using a fluorocarbon rubber O-ring. Two holes were drilled through the outer and inner lid to allow connecting tantalum tubes for mounting an overpressure valve on one tube and a sampling port and a manometer on the second tube. The tightness of the setup was tested prior to use in corrosion experiments. Each reactor has a total inner volume of 90 mL and was filled with 48 mL of solution in order to fully immerse the coupons. The total metallic surface of the coupons exposed to the solution was 9.50 $cm^2$, yielding a surface area to solution volume of 1:5 $cm^{-1}$ in all experiments. Experiments were performed in either 5 mol/L NaCl or 3.4 mol/L $MgCl_2$. Solutions were bubbled with Ar gas prior to their introduction in the Ar-filled box.

Corrosion experiments were performed at 25 °C or at 90 °C. For experiments performed at 90 °C, reactors were placed in holes drilled in thick metallic blocks to ensure homogeneous heating and mounted on electric heaters equipped with a sensor for temperature stabilization (± 2 °C). The whole setup was placed in a $N_2$-filled glovebox to avoid potential air ingress in case of unexpected loss of tightness. For experiments performed at room temperature, vessels were left in the $N_2$-filled glovebox without setup for heating. A separate Ar-filled glovebox was used for filling and closing the reactors, and for opening them after cooling at the end of the contact time. After cooling and opening, pH and $E_h$ were measured in situ and at room temperature before removing the coupons from the vessel. Following removal of the coupons from the vessel a fraction of the solution was ultracentrifuged (Beckman Coulter XL-90 K) for 30 min at 90,000 rpm before determining the concentration of dissolved metal ions by High-Resolution ICP-MS (Thermo Element XR). Coupons were quickly rinsed with deionized water and blown dry to get rid of the salt before analysis. Because only a limited number of experiments using these vessels could run in parallel in the anoxic glove box, coupons used for application of synchrotron-based techniques were prepared following the same procedure as described above, except that the used reactors were not fitted with manometer, sampling port and overpressure valve (lids were not drilled). For these experiments, reactors were closed in the Ar-filled glovebox and placed in an oven for 217 days at 90 °C not in any glovebox. At the end of the contact time, reactors were cooled and opened in the Ar-filled glovebox.

The pH was measured with a LL Solitrode combination electrode (Metrohm) calibrated with reference buffer solutions prior to measurements. Experimentally measured values were corrected for liquid junction potential effects and changes in activity coefficient of protons due to the ionic strength as described elsewhere [31]. All values mentioned in this study refer to molar concentrations of protons ($pH_M$). $pH_M$ corrections for temperature were performed with the PhreeqC software [32] using the ThermoChimie database [33] with the Specific Interaction Theory approach [34] and the amounts of dissolved metal ions determined by HR-ICP-MS. The uncertainty on $pH_M$ values at room temperature is typically < 0.1 unit, but is larger on the recalculated $pH_M$ values because of uncertainties associated with the quantification of amounts of dissolved metal ions. The redox potential (or $E_h$) was measured with a combination metal electrode having a Pt ring sensor and an Ag/AgCl reference (Radiometer Analytical). Values reported in this study are quoted with respect to the standard hydrogen electrode and have been used as input for the correction of $pH_M$ using PhreeqC. Measured $E_h$ values were not corrected for variations of liquid junction potential. Liquid junction potentials below 50 mV are expected in the conditions of this study [35], which are below uncertainties associated with $E_h$ measurements, and thus such corrections were disregarded in this work. Measured $E_h$ values were not corrected for temperature.

### 2.2. Analytical techniques

#### 2.2.1. Analysis of corroded surfaces

Anoxic conditions were ensured throughout the study by using appropriate transfer vessels and sample holders for the steel coupons. Before use in corrosion experiments, the average surface roughness of the polished coupons was estimated by analyzing one coupon by atomic force microscopy (AFM, Veeco Dimension 3100, Bruker). Results show that the original polished surface contains scratches of about 50 nm in depth (Fig. 1). Information on surface morphology and chemical composition of corroded coupons was obtained by scanning electron microscopy (SEM, Quanta 650 FEG, FEI) and energy dispersive X-ray spectroscopy (EDX, Thermo Scientific NORAN System 7 equipped with UltraDry™ silicon drift X-ray detector, Pathfinder X-ray microanalysis

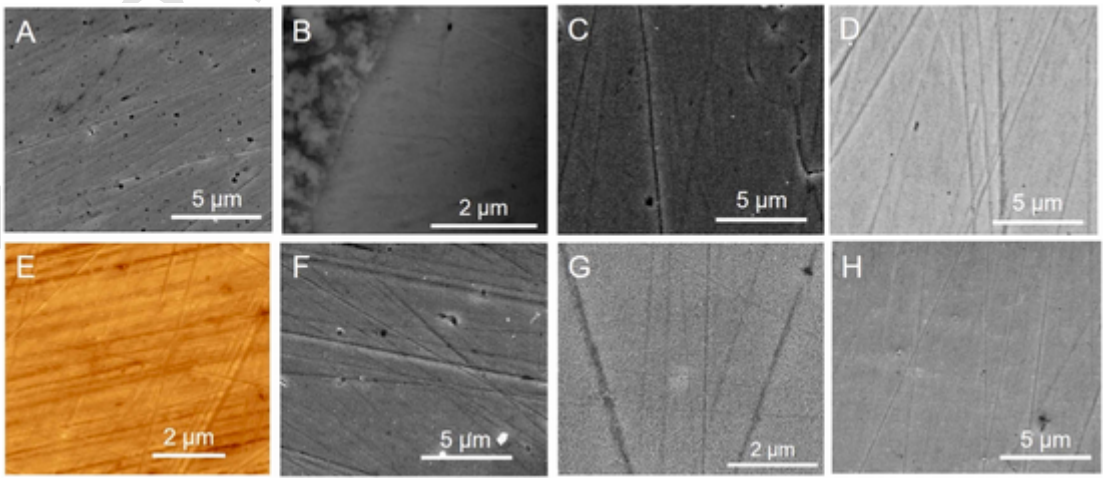


**Fig. 1.** Scanning electron micrograph (A) and AFM image (E) of a polished coupon before use in corrosion experiments. Electron micrograph after 182 d at 90 °C in 5 M NaCl (B) or in 3.4 M $MgCl_2$ (F), after 294 d at 90 °C in 5 M NaCl (C) or in 3.4 M $MgCl_2$ (G), and after 343 d at 25 °C in 5 M NaCl (D) or in 3.4 M $MgCl_2$ (H).

software v2.8). X-ray diffractograms were recorded using a D8 Advance diffractometer (Cu Kα radiation) equipped with a LynxEye XE-T detector (Bruker AXS). Measurements were performed in variable slits mode resulting in a constant illuminated surface of 12 mm (width) × 20 mm (length), independent of the 2θ angle. Data were treated using the DIFFRAC.EVA v5.0 software (Bruker AXS) and phase identification was performed using the PDF-2 database.

X-ray photoelectron spectroscopy (XPS, VersaProbe II, ULVAC-PHI, Al Kα (1486.7 eV) monochromatic X-ray excitation) was applied to analyze the elemental composition of the outermost layers. Specimens were mounted on the sample holder in the Ar-box and subsequently placed in a vacuum tight transfer vessel and closed inside the Ar-box. The transfer vessel was then attached to the introduction chamber of the instrument. The introduction chamber was evacuated and the transfer vessel opened, which allowed inserting the sample under strictly anoxic conditions. The data analysis was performed using the PHI MultiPak program v9.9. The calibration of the binding energy scale of the spectrometer was performed using well-established binding energies of elemental lines of pure metals (Cu $2p_{3/2}$ at 932.62 eV, Au $4f_{7/2}$ at 83.96 eV) [36]. The binding energies of elemental lines were charge-referenced to O 1 *s* of hydroxide at 531.4 eV as internal binding energy reference, comparable to charge referencing to C 1 *s* of hydrocarbon at 284.8 eV. Molar fractions of oxygen species were derived by curve fits to the O 1 *s* spectra by use of a Shirley background and Gaussian functions. The relative error of molar portions as determined is estimated to be within ± 10%, the error of binding energies of elemental lines is estimated to ± 0.2 eV. In the present study, relevant reference binding energies of O 1 *s* are 529.6 eV ($Fe_2O_3$), 530.0 eV ($Fe_3O_4$), 530.1 eV (FeO*OH) and 531.2 eV (FeOO*H), 531.0 eV ($Cr_2O_3$), 531.2 eV ($Cr(OH)_3$), and 531.4 eV (CrOOH) [37]. Relevant reference binding energies of the Cr $2p_{3/2}$ elemental lines are 576.9 eV ($Cr_2O_3$), 577.0 eV (CrOOH) and 577.3 eV ($Cr(OH)_3$) [37].

#### 2.2.2. Preparation and analysis of transversally cut samples

Corroded coupons prepared for synchrotron-based characterization techniques were embedded in epoxy resin (Buehler), transversally cut (Minitom, Struers) and polished with diamond-containing paste in an Ar-filled glovebox. Optical imaging for the selection of areas of interest on cross-sections was performed using a Zeiss Imager M2m microscope equipped with a CCD camera. SEM imaging was performed using a field emission gun apparatus (JEOL JSM7000-F) operated at 10 kV. Cross-sections were imaged in backscattered electron (BSE) mode with a 2 nA beam current. EDX spectra were recorded at points of interest using a silicon drift detector (Bruker XFlash 5010). Distribution maps of selected elements were recorded by continuous scanning of the sample and cumulative recording of EDX signal on each pixel.

Micro X-ray fluorescence (μXRF) spectroscopy, micro X-ray absorption near-edge structure (μXANES) spectroscopy and micro X-ray diffraction (μXRD) were performed at the DiffAbs beamline [38] at the SOLEIL synchrotron (Saint-Aubin, France). The storage ring was operated in uniform filling and top up mode, with a maximum stored current of 500 mA and an energy of stored electrons of 2.75 GeV. At the beamline, the energy of the incoming X-ray beam was selected using a fixed-exit monochromator equipped with a pair of Si < 111 > crystals and was calibrated by assigning the maximum of the first derivative of the Fe *K*-edge XANES spectrum recorded on an Fe foil to 7112.0 eV. The beam was focused down to 9 × 5 μm² (H × V, FWHM) using Kirkpatrick-Baez geometry type reflecting mirrors. For the measurements, the sample was encapsulated in an airtight holder with polyimide (Kapton®) windows and placed on the 6 + 2 circles diffractometer in kappa geometry. The sample was tilted horizontally by 10 ° off the perpendicular (angle χ) and the horizontal (angle Φ) orientations to the X-ray beam. Fast μXRF maps were recorded by scanning the sample with a 10 μm step size and 50 ms dwell time and monitoring the XRF signal using a 4 elements silicon drift detector (Vortex®-ME4, Hitachi). μXRF data were reduced and analyzed using the PyMCA XRF Toolkit [39]. The width and height of μXRF maps shown in the figures have different scales, the scale is represented as square on each map. Points of interest were selected to record μXRD data at an excitation energy of 8.4 keV using a 2D detector (XPAD S140 [40]). Additional points of interest were selected to record Cr, Fe and Ni *K*-edge μXANES spectra in fluorescence detection mode and were corrected for self-absorption using the Fluo algorithm implemented in the Athena interface to the Ifeffit software [41].

Solid reference compounds of known chemical composition (Table 2) were selected based on pre-characterization in the laboratory (e.g., SEM-EDX) of the corroded surfaces and the cross-sections. XANES spectra of these compounds (Supporting Information) were recorded either in transmission or in fluorescence yield detection mode at the Cr, Fe and/or Ni *K*-edge. XANES spectra of reference compounds were recorded either at the DiffAbs beamline at SOLEIL or at the INE Beamline [42] at the KIT Light Source (Karlsruhe Institute of Technology, Germany) using a standard beam size. At the KIT Light Source the energy of stored electrons was 2.5 GeV with a maximum stored current of 170 mA (no top up mode, one injection per day). At the INE Beamline, the energy of the impinging X-ray beam was selected using a fixed-exit monochromator equipped with a pair of Si < 111 > crystals and was calibrated by using either a Cr, Fe or Ni foil measured in parallel. At this beamline a combination of two silicon drift detectors, a Vortex®-ME4 (4 elements) and a Vortex®−60EX (1 element) (Hitachi/SIINT), was used to record data in fluorescence yield detection mode.

Data reduction of XANES spectra involved energy calibration, background subtraction and normalization. Analyses were performed using Linear Combination Fitting (LCF) with the Athena interface to the Ifeffit software [41]. LCF was used to reconstruct the sample spectrum using a combination of selected model spectra within the energy range of − 20 eV below to + 80 eV above the edge. The fit quality was quantified by the residual factor ($R_f$) indicating the absolute misfit between theory and data. The uncertainty on the percentage that each model compound contributes to the fit is indicated in parentheses in the corresponding tables.

## 3. Results

### 3.1. Analyses of the fluids

#### 3.1.1. Gas phase

Heating the reactors to 90 °C resulted in an increase of the pressure by 0.7 bar inside the vessels due to the increase of the vapor pressure of water [43]. The pressure remained constant over time, but decreased slightly after about 60 days in some experiments. These results suggest a loss of tightness and possible escape of hydrogen gas produced by cor-

**Table 2**
Reference compounds used in Linear Combination Analysis of μXANES spectra (LDH: layered double hydroxide).

| Reference compound | Composition | Probed *K*-edge |
|---|---|---|
| Chromium oxide | $Cr_2O_3$ | Cr |
| Chromium hydroxide | $Cr(OH)_3$ | Cr |
| Cr-doped magnetite | $Fe_{2.8}Cr_{0.2}O_4$ | Cr, Fe |
| Chromite | $FeCr_2O_4$ | Cr, Fe |
| Magnetite | $Fe_3O_4$ | Fe |
| Fe-LDH (green rust) | $[Fe_4(OH)_8]$ $[Cl•nH_2O]$ | Fe |
| Ferrous hydroxychloride | $β\text{-}Fe_2(OH)_3Cl$ | Fe |
| Wüstite | FeO | Fe |
| Hematite | $α\text{-}Fe_2O_3$ | Fe |
| Akaganeite | β-FeOOH | Fe |
| Trevorite | $NiFe_2O_4$ | Fe, Ni |
| Nickel oxide | NiO | Ni |
| Nickel hydroxide | $Ni(OH)_2$ | Ni |
| CrFeNi-LDH | $[Fe_{2.3}Ni_{0.6}Cr_{1.1}(OH)_8]$ $[Cl•nH_2O]$ | Cr, Fe, Ni |
| Steel | $Cr_{0.43}Mn_{0.02}Fe_{1.13}Ni_{0.22}$ | Cr, Fe, Ni |

rosion processes. Performing experiments inside an anoxic glovebox avoided the diffusion of oxygen into the vessels and thus anoxic conditions were ensured. Analyzing the gas phase using the sampling port was consequently not performed. No pressure increase could be detected for experiments performed at room temperature. Note, however, that the observed corrosion rates (see discussion below) were low and not much hydrogen evolution can be expected.

### 3.1.2. $pH_M$ and redox potential

In 5 M NaCl brines, the $pH_M$ hardly changed for experiments performed at 25 °C while it increased by one unit at 90 °C (Fig. 2). At elevated temperature in concentrated $MgCl_2$ solutions, the $pH_M$ hardly varied for 294 days of contact time, but it slightly increased after 343 days at 25 °C. The redox potential decreased only in 5 M NaCl at 90 °C, in all other experiments it was not lower than + 100 mV. Compared to reported evolutions of $E_h$ in corrosion experiments (e.g. [26]), the observed evolution of $E_h$ in 5 M NaCl at 90 °C would be consistent with ongoing corrosion. Thus in the other systems, the extent of corrosion and corrosion rates may be lower. Redox conditions in our experiments will be discussed in more detail below.

### 3.1.3. Concentration of dissolved metal ions

The determined amounts of dissolved metal ions were often close to the detection limit because contacting brines were highly diluted to permit HR-ICP-MS analysis (Table 3). The lowest concentrations of metal ions were obtained for chromium, followed by iron and the highest values were obtained for Ni. This trend follows the solubility of the (hydr)oxide phases forming from the dissolved metal ions [44]. The concentrations of dissolved Fe and Ni in experiments performed at 90 °C initially increased and then decreased, suggesting the formation of secondary phases after some kind of induction phase.

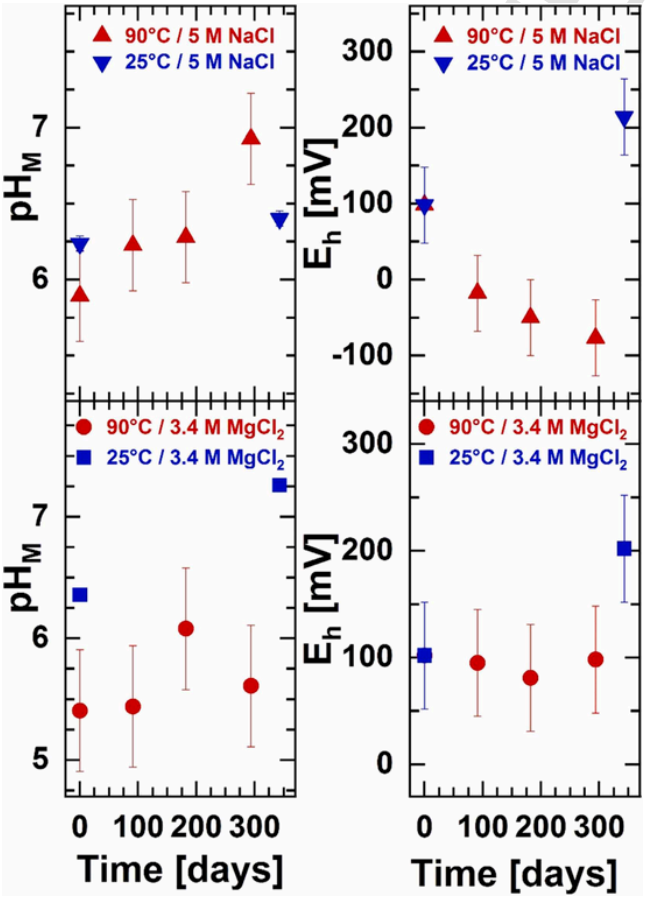


**Fig. 2.** $pH_M$ and redox potential ($E_h$) evolutions in the corrosion experiments.

**Table 3**
Dissolved amounts (µg/L) of metal ions in the corrosion experiments. Numbers in parentheses indicate the relative standard deviation in %.

| Systems | 91 days | 182 days | 294 days | 343 days |
|---|---|---|---|---|
| | Cr | | | |
| **90 °C / 5 M NaCl** | < 10 | 41 (47) | < 10 | - |
| **25 °C / 5 M NaCl** | - | - | - | < 10 |
| **90 °C / 3.4 M $MgCl_2$** | 31 (22) | < 10 | < 10 | - |
| **25 °C / 3.4 M $MgCl_2$** | - | - | - | < 10 |
| | **Fe** | | | |
| **90 °C / 5 M NaCl** | 12 (29) | 61 (15) | < 10 | - |
| **25 °C / 5 M NaCl** | - | - | - | < 10 |
| **90 °C / 3.4 M $MgCl_2$** | 91 (44) | 1099 (4) | < 10 | - |
| **25 °C / 3.4 M $MgCl_2$** | - | - | - | < 10 |
| | **Ni** | | | |
| **90 °C / 5 M NaCl** | 228 (2) | 797 (4) | < 30 | - |
| **25 °C / 5 M NaCl** | - | - | - | < 30 |
| **90 °C / 3.4 M $MgCl_2$** | 111 (22) | 542 (4) | < 30 | - |
| **25 °C / 3.4 M $MgCl_2$** | - | - | - | < 30 |

## 3.2. Surface analysis of corroded samples

The corroded coupons have a relatively limited surface damage (Fig. 1). Electron micrographs show the presence of a small deposit of fine-grained material on the surface, but the amount is not always increasing with contact time. It is very likely that the procedure used to remove the salt also removed a fraction of neoformed corrosion products. The surface of several corroded coupons exhibits scratches very similar to that of the original polished sample, which agrees with a very limited surface attack. Low amounts of fine-grained material covering the surface or a fraction of it can only be seen on the coupon after contacting the 5.0 M NaCl brine at 90 °C for 182 days and that contacting the 3.4 M $MgCl_2$ brine at 90 °C for 294 days. The bright spots on the micrograph of the coupon exposed to 3.4 M $MgCl_2$ at 90 °C for 182 days may likely correspond to salt crystals.

X-ray diffraction was first applied to get insight into the nature of the deposits (Fig. 3). The diffractogram of all corroded coupons compare well with that of the starting non-corroded coupon meaning that the amount of fine-grained deposits was too low for identifying their mineralogical nature using this technique. The starting austenitic steel crystallizes in the face-centered cubic (fcc) structure of γ-Fe. A closer look at the high angular side of the most intense reflection corresponding to the (111) plane reveals the presence of a low intensity reflection not originating from this structure. Instead, this reflection may suggest the presence of α-Fe crystallizing in body-centered cubic (bcc) configuration and which crystal structure has slightly smaller unit cell parameters. The ferritic structure of α-Fe is thermodynamically stable below about 910 °C and undergoes a phase transition above this temperature to the fcc configuration of γ-Fe. The fcc structure is stable only above 910 °C, but it can be stabilized at room temperature by adding high amounts of alloying elements such as Ni (13.17 wt% Ni, Table 1). The presence of high amounts of Cr (22.45 wt%) in 309 S confers good corrosion resistance, but it also tends to destabilize the fcc structure and to promote the bcc structure. Indeed, austenitic 304 and 316 stainless steels can contain a certain amount of bcc structure, depending on production and processing [45,46]. The amount of α-Fe present in the initial 309 S seems marginal, but diffractograms suggest the presence of low amounts of this allotrope in the corroded samples. The origin of this finding is still unclear.

XPS analysis of the coupons revealed the presence of a Cr(III)-rich layer covering the surface (Fig. 4, Supporting Information). Based on the reported O 1 *s* binding energy of various reference compounds [37], the analyses of the spectra indicate that in all samples the layer consists

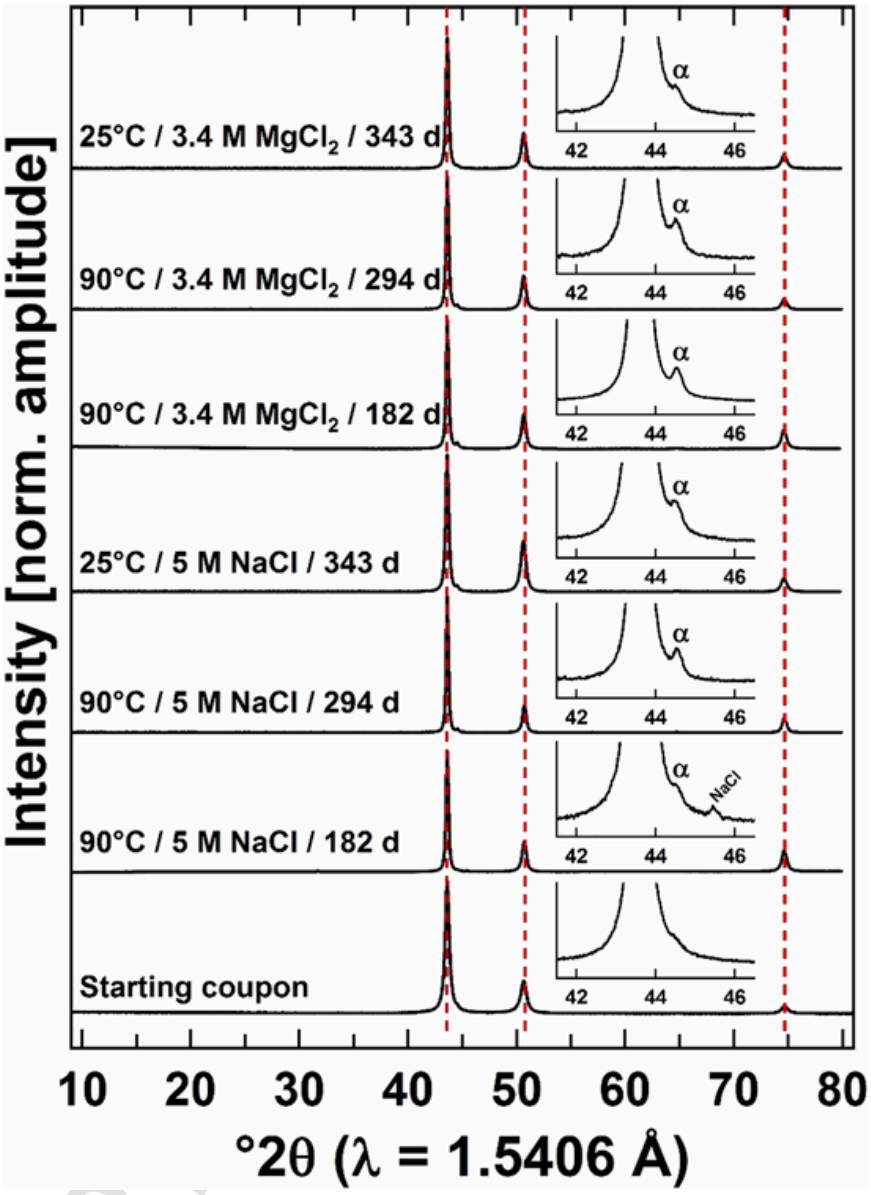


**Fig. 3.** X-ray diffractogram of the starting coupon and of selected samples corroded in concentrated NaCl or $MgCl_2$ brine. Dashed red vertical lines represent positions of reflections for the face-centered cubic structure of γ-Fe (austenite) (PDF 33–0397). Inserts show the presence of a low intensity reflection hinting at the presence of α-Fe in the corroded coupons. No presence of corrosion product can be evidenced.

of a mixture of oxide (around 530.0 eV) and hydroxide (531.4 eV), with a minor hydrate contribution (around 532.8 eV) (Fig. 4, Table 4).

For specimens exposed to 5 M NaCl at 90 °C, the portion of oxidic bonds is almost constant at about 27–30 mol% up to 294 days (Table 4). The portion of hydrate slightly decreases from 14 mol% after 182 days to 8 mol% after 294 days and the portion assigned to hydroxide concomitantly increases from 56 mol% to 65 mol%. The modest increase of hydroxide species may possibly be explained by the slight $pH_M$ increase. The portion of hydroxide bonds also dominates with 63 mol% after 343 days at 25 °C and the portions of oxidic and hydrate are comparable with 18–19 mol%.

The portion and evolution with contact time of hydroxide bonds are similar in $MgCl_2$ and in NaCl brines at 90 °C (Table 4). A decrease of the portion of oxidic bonds from 30 mol% after 182 days to 14 mol% after 294 days in the $MgCl_2$ brine is balanced by an increase of hydrate bonds. After 343 days at 25 °C the portion of hydroxide bonds also dominates with 54 mol% and the portion of oxidic bonds represents 30 mol%.

In both brines at 90 °C the portion of hydroxide bonds dominates and the portion of oxidic bonds decreases with contact time (Table 4). The portion of hydroxide bonds also dominates at 25 °C in both brines but the portion of oxidic bonds is significantly larger in the $MgCl_2$ brine. Because of the high surface sensitivity of XPS the observed differences may best be attributed to dissimilarities in the contacting brines.

Unfortunately, reported binding energies of the Cr $2p_{3/2}$ elemental lines of Cr (hydr)oxides are very close to each other [37], which makes it difficult to specify the portions of chromium compounds. This issue is compounded by line broadening due to splitting of Cr(III) 2*p* (Supporting Information). However, the estimation of the portions of chromium species was attempted by fits to the experimental spectra according to reported procedures [47]. In both brines, spectra and atomic concentrations indicate the presence of iron and an enhanced abundance of chromium (hydr)oxides at the surface exposed to the brines, which supports the well-known formation of a protective Cr-rich layer at the steel/brine interface. It is obvious that the presence of corrosion phases is limited after the relatively short time of our experiments.

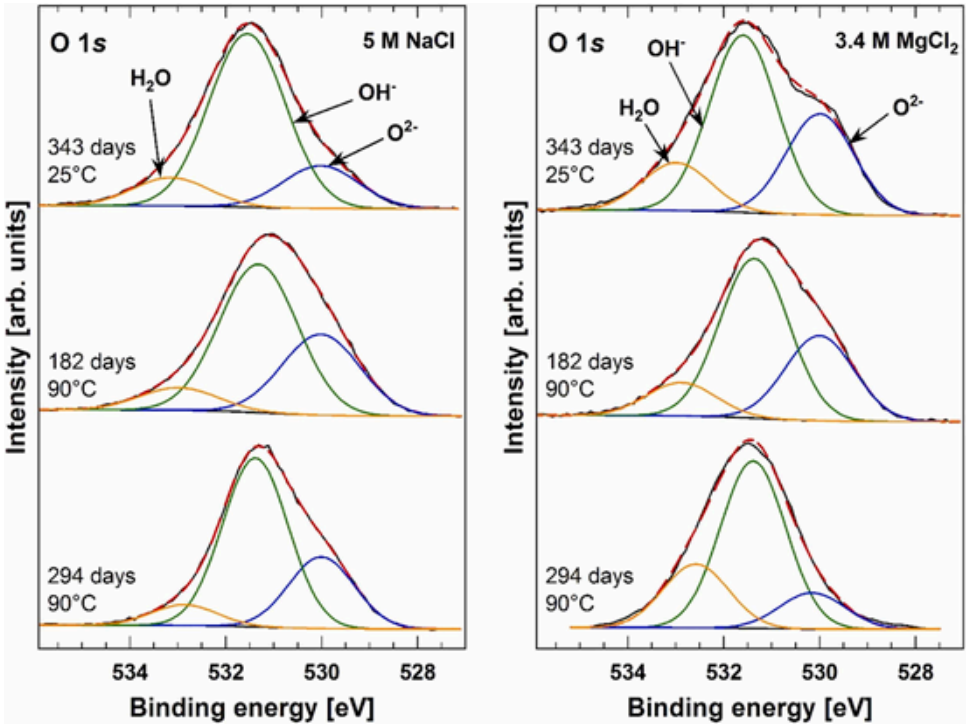


**Fig. 4.** Experimental (black solid lines) and modeled (red dashed lines) narrow O 1 *s* X-ray photoelectron spectra of samples corroded in either 5 M NaCl (left) or 3.4 M $MgCl_2$ (right), at 25 °C (top) or at 90 °C (middle, bottom). Contributions of hydrate, hydroxide and oxidic bonds are indicated in orange, green and blue, respectively. Fit results are presented in Table 4.

**Table 4**
Molar percentages of oxygen bonding obtained by curve fitting to the narrow O 1 *s* X-ray photoelectron spectra (Fig. 4) by use of a Shirley background and Gaussian functions. Relative errors are estimated to be within ± 10%.

| Systems | 5 M NaCl | | | 3.4 M $MgCl_2$ | | |
|---|---|---|---|---|---|---|
| | $H_2O$ | $OH^-$ | $O^{2-}$ | $H_2O$ | $OH^-$ | $O^{2-}$ |
| **25 °C, 343 days** | 18 | 63 | 19 | 16 | 53 | 31 |
| **90 °C, 182 days** | 14 | 56 | 30 | 13 | 57 | 30 |
| **90 °C, 294 days** | 8 | 65 | 27 | 24 | 62 | 14 |

However, results show the stability of Cr oxide/hydroxides as corrosion phases in brine solutions, which may become dominant after the relevant long time scales in a HLRW repository.

### 3.3. Analysis of transversally cut samples

#### 3.3.1. Optical overview and scanning electron microscopic analyses

For the sample corroded in 5 M NaCl at 90 °C, the optical overview of the transversal cut shows the presence of a very thin and heterogeneous layer (Fig. 5). This sample was selected for further analyses. For the coupon corroded in concentrated $MgCl_2$ brine at 90 °C the layer was also heterogeneous and even thinner (not shown), hindering further analyses.

For the specimen corroded in 5 M NaCl, the electron micrograph in BSE mode suggests that the corrosion layer cracked and detached from the surface during sample preparation and adhered to the resin (Fig. 5). The corrosion layer itself is very thin (from the micrograph it can be estimated to be around 1 µm or less). The gap between the detached layer and the steel surface is rather important at the transversally cut surface and decreases for increasing distance from this cut surface, suggesting that the detachment occurred during the cutting of the embedded coupon.

The surface of the detached corrosion layer is mostly made of Cr and contains lower amounts of Fe and Ni (Fig. 5). The oxygen content of this layer seems larger at the cut surface. Several points were selected for quantitative EDX analysis (Table 5). The composition at point 5 nearly matches the composition of the starting non-corroded coupon. At points 1 and 4, the O content is high, the Cr content is significant and the Fe and Ni contents are moderate. Atomic ratios suggest the presence of a mixture of oxide and/or hydroxide of transition metal elements. At these positions, the relative proportion of Cr is larger than that in the starting steel, while proportions of Fe and Ni are lower. Results may thus point at the prevalence of chromium oxide/hydroxide, which has already been observed by XPS (Section 3.2). The low O content detected at points 2 and 3, where the corrosion layer was in contact with the steel surface, excludes the presence of oxide and/or hydroxide compounds in significant amounts and instead may suggest the presence of metallic particles. However, the relative proportions of Cr, Fe and Ni significantly differ from that of the original 309 S and rather hint at an alloy predominantly made of Cr. The origin of this result is unclear, but it could possibly correspond to inhomogeneity of the starting steel or to an alteration of the composition induced by corrosion. The observed heterogeneity in distribution of elements within the corrosion layer precludes the identification of the exact nature of formed corrosion products based on EDX analysis alone. Element specific spectroscopic techniques were further applied to add constraints in the identification of the nature of formed secondary phases.

#### 3.3.2. Microspectroscopic analyses

µXRF spectroscopy was first applied to obtain the spatial distribution of elements and to select points of interest for a detailed structural analysis. Elemental maps corroborate the presence of a thin layer on the surface of the coupon with a composition differing from that of the bulk steel (Fig. 6). Ni and Cr accumulated in some regions of the layer. For example, the area on the right side is Cr-rich, Fe-poor and has a moderate Ni content. In contrast, the Cr content is low and the Ni content is high at the center and left side. These trends are corroborated by drawing a correlation map with a color-code for each element. The reddish or pink color on the right indicates a dominant Cr content, and when

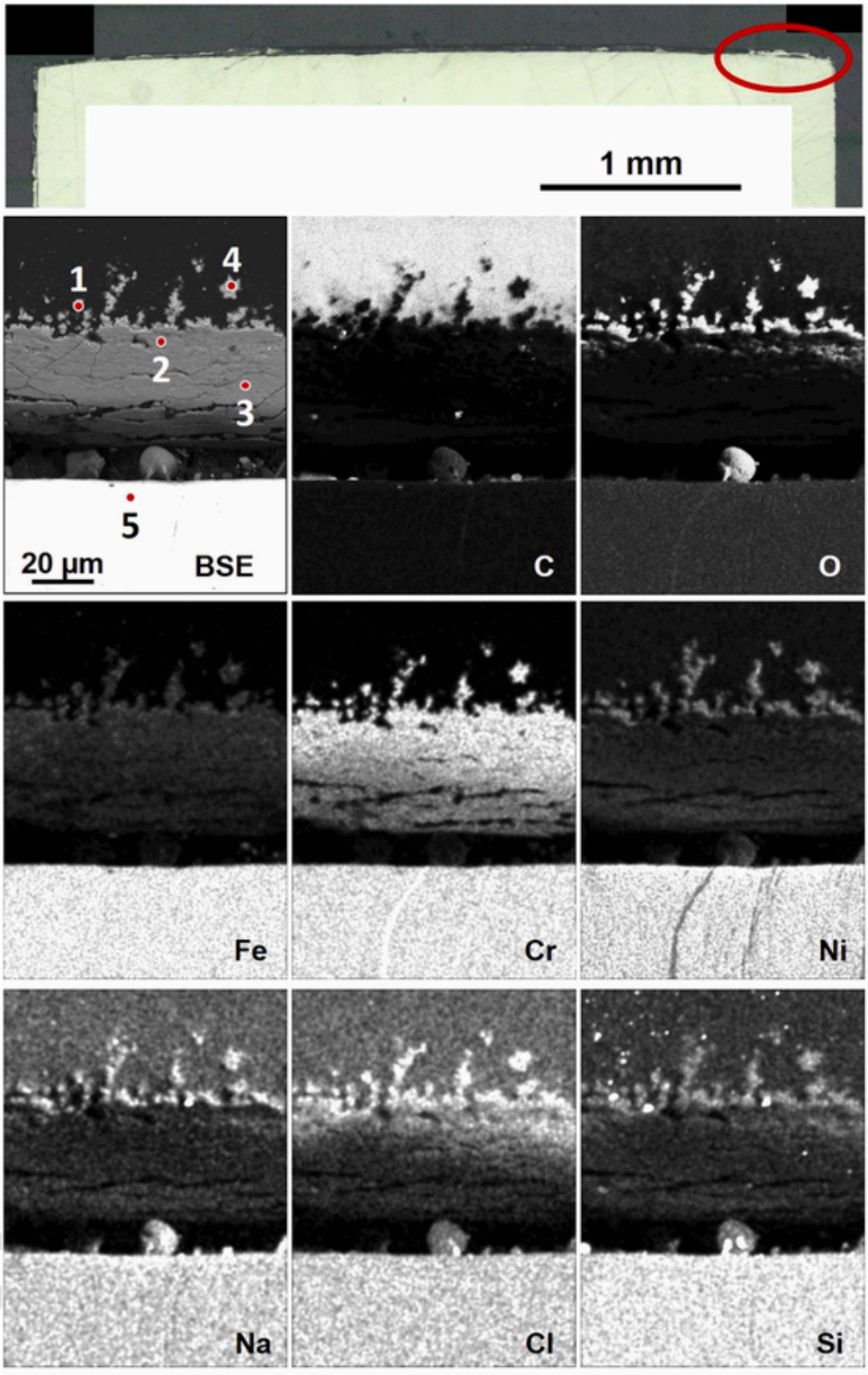


**Fig. 5.** Top: Optical image of the transversally cut sample used in the microspectroscopic analysis. Middle, bottom: backscattered electron (BSE) image and EDX element maps of the corrosion interface selected at the top right side of the coupon. Bright areas correspond to high concentrations. The BSE image also shows the locations of points selected for quantitative EDX analyses (Table 5).

moving to the left, the transition to green and blue reveals predominant Fe and Ni contents, respectively. These findings are in agreement with the BSE image and elemental EDX maps showing a detachment of the corrosion layer on the right side and with the detected high Cr content in the corrosion layer detached from the coupon. All these findings show that Cr and Ni enrichment is apparently quite heterogeneous with different relative contents within the corrosion layer.

Micro X-ray diffractograms were subsequently recorded in order to identify the structure of the corrosion products. Points of interest were first selected in the corrosion layer in areas where Fe and Ni proportions are highest (Fig. 7). The presence of magnetite is detected at points D

**Table 5**
Quantification of EDX analyses at selected points of interest indicated in Fig. 5. Relative errors are estimated to be within ± 10%.

| Point of interest | Composition (at%) | | | | | | | | |
|---|---|---|---|---|---|---|---|---|---|
| | O | Na | Mg | Al | Si | Cl | Cr | Fe | Ni |
| **1** | 58.1 | 0.6 | 0.1 | 0.1 | 0.7 | 1.6 | 28.6 | 7.6 | 2.6 |
| **2** | 3.2 | 0 | 0 | 0 | 0.3 | 1.7 | 69.8 | 23.5 | 1.5 |
| **3** | 3.6 | 0.3 | 0.1 | 1.0 | 0.5 | 0.7 | 63.5 | 25.7 | 4.7 |
| **4** | 61.2 | 1.4 | 0.1 | 0.1 | 0.7 | 1.9 | 22.4 | 7.0 | 5.2 |
| **5** | 3.9 | 0.9 | 0.6 | 0.5 | 1.0 | 0 | 22.7 | 58.2 | 12.3 |

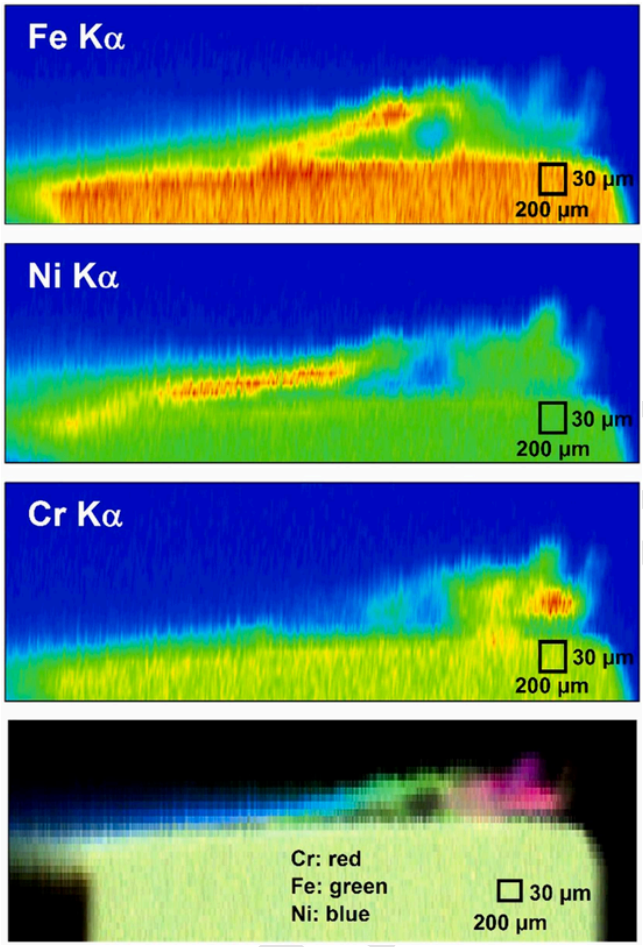


**Fig. 6.** µXRF maps (excitation energy: 8.4 keV) showing the distribution of Fe, Ni and Cr for the corroded sample (color concentration scale: red = high concentration, green/blue = low concentration). The bottom map shows the correlation obtained by associating one color to one element.

and E close to the steel. Given the comparable atomic radii of Cr, Fe and Ni, a (small) fraction of Fe in magnetite may also be replaced by Ni and/or Cr. Trevorite ($NiFe_2O_4$) and chromite ($FeCr_2O_4$) are both isostructural with magnetite, and could also form as corrosion products. However, the Cr content at these points is very low, ruling out the formation of chromite in significant amounts. The simultaneous presence of magnetite and trevorite cannot be assessed unambiguously based on µXRD analysis alone, but no other Ni-bearing phase was detected in significant amounts and the presence of $NiFe_2O_4$ would agree with the detected substantial Ni content. The nature of phases detected at point C is comparable to that detected at point E (mostly magnetite and/or trevorite). Diffractograms also point to the presence of hematite (α-$Fe_2O_3$) at points B and A. The presence of α-$Fe_2O_3$ is not expected in experiments performed under anoxic conditions and could be caused by

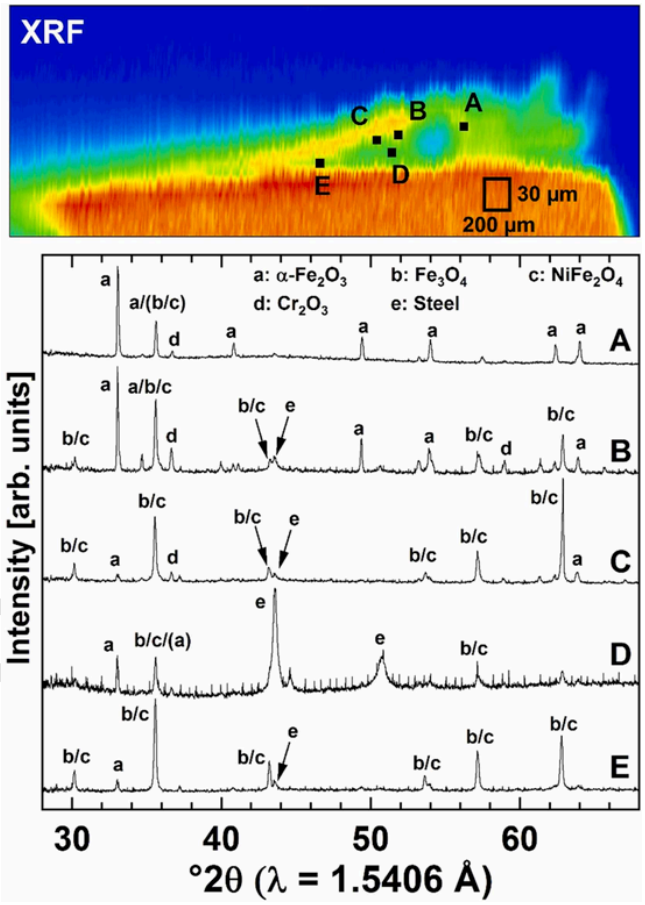


**Fig. 7.** Micro X-ray diffractograms recorded at various locations in the corrosion layer as shown on the µXRF map (excitation energy: 8.4 keV, total recorded signal (Cr Kα + Fe Kα + Ni Kα)).

the presence of residual oxygen left from preparing the experiment. We can, however, not totally exclude oxygen access during the time where reactors were placed in the oven outside of the $N_2$-filled glovebox. Note that $Fe^{3+}$ and $Cr^{3+}$ have very similar ionic radii implying that chromic ions may substitute for ferric ions in various amounts within hematite and form a $Fe_{2-x}Cr_xO_3$ solid solution. Finally, most diffractograms also evidence the presence of $Cr_2O_3$, which forms readily as passivation layer on stainless steel. Other phases may also be present but could not be identified either because of their low amounts or because of their low crystallinity. µXANES measurements were performed to provide complementary information, especially on Fe and Ni local environments.

Several points were selected to probe both the Fe and the Ni *K*-edges by XANES in areas where the corrosion layer displays high contents in these elements. This strategy allows adding further constraints on the structure of the corrosion products. At points Fe7/Ni7 and Fe8/Ni8, where the corrosion layer is closest to the steel (Fig. 8, Table 6), the presence of spinel-type compounds magnetite and trevorite was identified with a contribution of 15–20% to the XANES. Further to the right (Fe6, Fe5, Fe4), only increasing proportions of magnetite could be detected in addition to steel when probing the Fe *K*-edge. At these same positions Ni *K*-edge µXANES spectra (Ni3-Ni6) reveal the presence of trevorite in proportions ranging from 20% to 50%, while the presence of steel was only detected at positions Ni3 and Ni4 (about 60%). Interestingly, data also hint at the presence of NiO and $Ni(OH)_2$ (Ni6, Ni5 and Ni4), which were not detected by µXRD. Actually, reflections of NiO would be expected at 2θ values of ~43.3° and ~62.9° but they overlap with reflections of Fe/Ni spinel-type compounds, only the weak

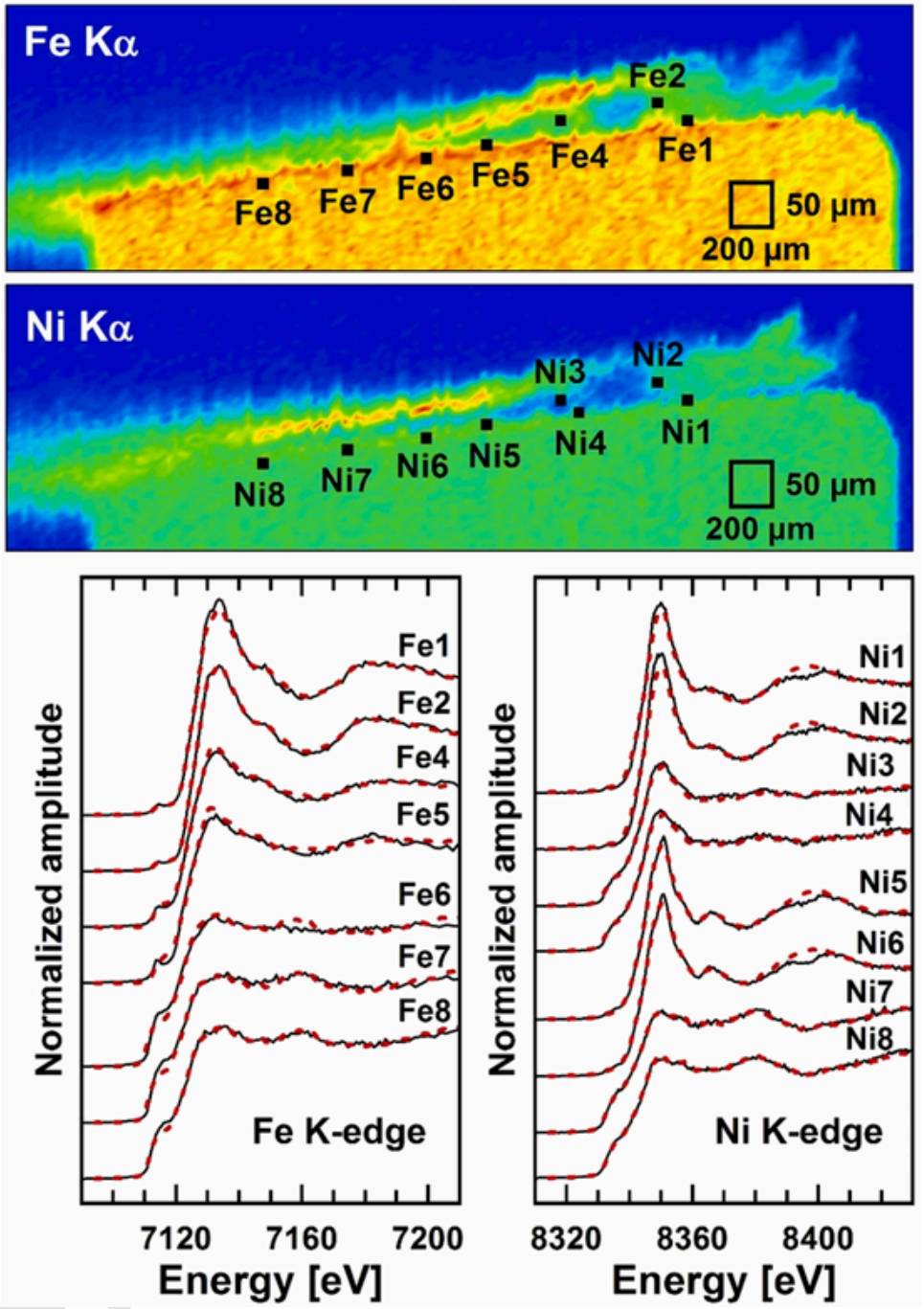


**Fig. 8.** Experimental (solid black line) and modeled (dashed red line) Fe *K*-edge and Ni *K*-edge µXANES spectra recorded in the corrosion layer at some points of interest marked on the µXRF maps (excitation energy: 8.4 keV). Quantitative results of fits to the µXANES spectra are presented in Table 6.

reflection at ~37.2° on the diffractogram recorded at position C could indicate the presence of NiO in minor amounts. Similarly, the reflection at ~33.2° attributed to the presence of α-$Fe_2O_3$ may also hint at the presence of $Ni(OH)_2$. Interestingly, CrFeNi-LDH (layered double hydroxide containing Cr, Fe and Ni) was detected in substantial amounts at position Ni3 and as the only phase at points Ni2 and Ni1. The Fe *K*-edge XANES data also indicate the presence of CrFeNi-LDH at positions Fe1 and Fe2, but only in very low amounts, the majority of Fe being present as α-$Fe_2O_3$ or as $Fe_{2-x}Cr_xO_3$. The substitution of Cr for Fe within α-$Fe_2O_3$ would not significantly change the spectroscopic signature because backscattering from Cr and Fe are very comparable. The detection of (Cr-doped) α-$Fe_2O_3$ agrees with µXRD analysis, but the presence of LDH was not detected on diffractograms possibly because of its low content or poor crystallinity.

The second study area was the right side of the corroded interface, where the corrosion layer detached from the surface. X-ray diffractograms recorded at several positions on a line going from the pristine steel to the resin (Fig. 9) evidence a transition from steel (point H) to α-$Fe_2O_3$ present in the layer detached from the surface (points I and J). Taking into account results from µXRF analysis (Fig. 6), the compound detected in the corrosion layer may most likely be Cr-rich and Fe-poor $Fe_{2-x}Cr_xO_3$. No other corrosion product could be detected in the area. Diffractograms recorded at points F, G and H exhibit an additional weak reflection at ~44.5° that was also present on diffractograms recorded in the laboratory (Fig. 3). This result suggests the presence of

**Table 6**
Mineralogical composition (mol%) as obtained by linear combination fits to the Fe K-edge and Ni K-edge μXANES spectra recorded at selected points shown in Fig. 8. Uncertainties are indicated in parentheses.

| Point of interest | Results of linear combination fitting (mol%) | $R_f$ ($\times 10^3$) |
|---|---|---|
| | **Fe *K*-edge** | |
| **Fe1** | 96(5) % $\alpha$-$Fe_2O_3$ + 4(5) % CrFeNi-LDH | 3.0 |
| **Fe2** | 92(3) % $\alpha$-$Fe_2O_3$ + 8(4) % CrFeNi-LDH | 1.1 |
| **Fe4** | 26(2) % steel + 74(2) % Cr-doped $Fe_3O_4$ | 3.1 |
| **Fe5** | 36(2) % steel + 64(2) % Cr-doped $Fe_3O_4$ | 8.0 |
| **Fe6** | 74(2) % steel + 26(2) % Cr-doped $Fe_3O_4$ | 8.8 |
| **Fe7** | 84(2) % steel + 16(2) % Cr-doped $Fe_3O_4$ | 5.9 |
| **Fe8** | 80(2) % steel + 20(2) % $NiFe_2O_4$ | 2.8 |
| | **Ni *K*-edge** | |
| **Ni1** | 100% CrFeNi-LDH | 8.4 |
| **Ni2** | 100% CrFeNi-LDH | 10.4 |
| **Ni3** | 57(7) % steel + 22(5) % $NiFe_2O_4$ + 21(5) % CrFeNi-LDH | 2.5 |
| **Ni4** | 56(8) % steel + 23(6) % $Ni(OH)_2$ + 21(5) % $NiFe_2O_4$ | 2.9 |
| **Ni5** | 43(5) % $Ni(OH)_2$ + 34(14) % NiO + 23(10) % $NiFe_2O_4$ | 5.3 |
| **Ni6** | 53(10) % $Ni(OH)_2$ + 47(7) % $NiFe_2O_4$ | 7.7 |
| **Ni7** | 86(2) % steel + 14(2) % $NiFe_2O_4$ | 1.3 |
| **Ni8** | 85(2) % steel + 15(2) % $NiFe_2O_4$ | 0.9 |

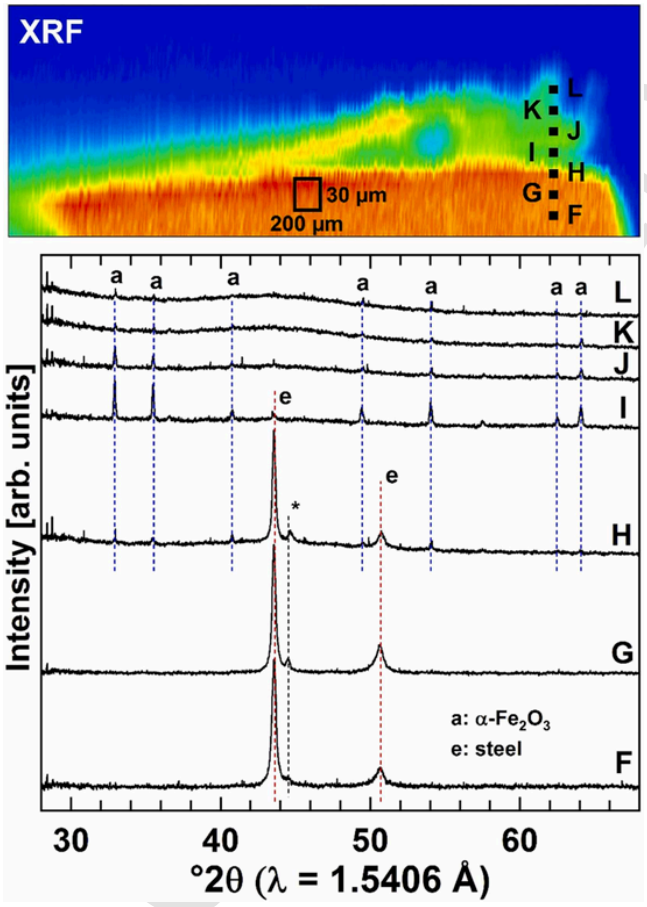


**Fig. 9.** Micro X-ray diffractograms recorded through the corrosion layer in the Cr-rich region at positions shown on the μXRF map (excitation energy: 8.4 keV, total recorded signal (Cr Kα + Fe Kα + Ni Kα)). The asterisk indicates position of a reflection possibly corresponding to α-Fe.

an additional minor phase, very likely α-Fe, present within the steel just below the surface because the intensity of the reflection decreases with distance from the metallic surface/corrosion layer interface.

As not all secondary phases may be crystalline, Cr *K*-edge μXANES spectra were recorded at points of interest selected in the same area. The presence of Cr-containing $Fe_3O_4$ was detected at all selected points (Fig. 10, Table 7). This was the only phase detected at point Cr9, which is closest to the region having a high Fe content. At point Cr5, which is close to point Cr9 and to the steel surface, a fraction of Cr is structurally bound to LDH, consistent with the analysis of Fe and Ni *K*-edge μXANES recorded at point Fe1/Ni1 located in close proximity. At all other positions, $Cr(OH)_3$ was detected, sometimes admixed with $Cr_2O_3$, which are

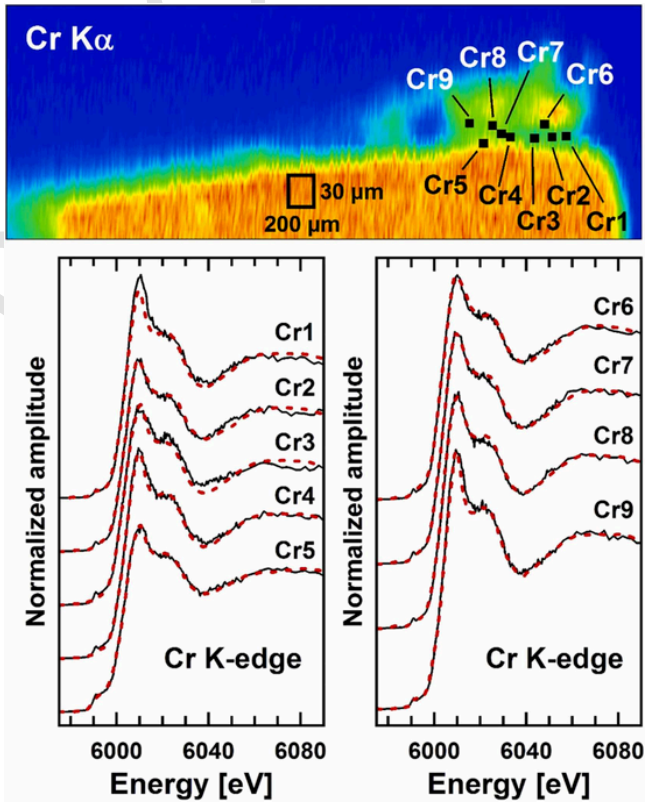


**Fig. 10.** Experimental (solid black line) and modeled (dashed red line) Cr *K*-edge μXANES spectra recorded in the corrosion layer at some points of interest marked on the μXRF map (excitation energy: 6.2 keV). Quantitative results of fits to the μXANES spectra are presented in Table 7.

**Table 7**
Mineralogical composition (mol%) as obtained by linear combination fits to the Cr K-edge μXANES spectra recorded at selected points shown in Fig. 10. Uncertainties are indicated in parentheses.

| Point of interest | Results of linear combination fitting (mol%) | $R_f$ ($\times 10^3$) |
|---|---|---|
| **Cr1** | 69(10) % Cr-doped $Fe_3O_4$ + 31(9) % $Cr(OH)_3$ | 6.4 |
| **Cr2** | 41(6) % Cr-doped $Fe_3O_4$ + 24(6) % $Cr(OH)_3$ + 35(9) % $Cr_2O_3$ | 2.0 |
| **Cr3** | 57(9) % Cr-doped $Fe_3O_4$ + 43(5) % $Cr(OH)_3$ | 5.5 |
| **Cr4** | 73(4) % Cr-doped $Fe_3O_4$ + 27(4) % $Cr(OH)_3$ | 2.4 |
| **Cr5** | 60(2) % Cr-doped $Fe_3O_4$ + 23(2) % CrFeNi-LDH + 17(2) % steel | 1.3 |
| **Cr6** | 28(5) % Cr-doped $Fe_3O_4$ + 22(5) % $Cr(OH)_3$ + 50(7) % $Cr_2O_3$ | 1.3 |
| **Cr7** | 31(4) % Cr-doped $Fe_3O_4$ + 34(4) % $Cr(OH)_3$ + 35(2) % $Cr_2O_3$ | 0.9 |
| **Cr8** | 23(6) % Cr-doped $Fe_3O_4$ + 52(7) % $Cr(OH)_3$ + 25(2) % $FeCr_2O_4$ | 1.1 |
| **Cr9** | 100% Cr-doped $Fe_3O_4$ | 2.7 |

phases typically present in the passivation layer of stainless steel. No significant difference in nature of Cr-bearing phase can be evidenced when comparing points closer to the surface with those further away. Here also the presence of $Fe_{2-x}Cr_xO_3$ instead of pure $Cr_2O_3$ can be assumed, as well as $Fe^{3+}$ substituting for $Cr^{3+}$ within $Cr(OH)_3$. The substitution of $Fe^{3+}$ for $Cr^{3+}$ is very likely and would not necessarily be detected by μXANES. The detection of Cr (hydr)oxide within the layer agrees with results from XPS analysis. Neither spinel-type compounds (e.g., magnetite) nor pure chromium (hydr)oxide detected by μXANES could be detected by μXRD analysis in this region, possibly because of their poor crystallinity.

## 4. Discussion

### 4.1. Corrosion mechanism

The relatively high Cr content of 309 S results in the formation of a protective film upon contact with air during the preparation of the samples, even before the start of the corrosion experiments. When immersed in brines, the Cr-rich film further develops on the surface because chromium has the lowest oxidation potential among all elements constitutive of the alloy (Table 8). Under these conditions, the formation of chromium hydroxide is favored over the formation of the oxide because of lower standard free energy following [48]:

$$Cr_{(m)} + 3OH^- \rightarrow Cr(OH)_{3(s)} + 3e^- \quad (1)$$

The concomitant cathodic water reduction provides hydroxide ions:

$$2H_2O + 2e^- \rightarrow 2OH^- + H_{2(g)} \quad (2)$$

A fraction of chromium hydroxide is subsequently converted into chromium oxide by combining with inward diffusing $OH^-$ and outward diffusing metallic Cr [49,50]:

$$Cr(OH)_{3(s)} + Cr_{(m)} + 3OH^- \rightarrow Cr_2O_{3(s)} + 3H_2O + 3e^- \quad (3)$$

The presence of this oxide layer protects the surface and prevents the diffusion of other metallic ions from the metallic surface to the brine. However, the film has pores and defects, allowing Fe and Ni to be transported through the oxide film and to react with hydroxide ions at the solid/solution interface:

$$Fe^{2+} + 2OH^- \rightarrow Fe(OH)_{2(s)} \quad (4)$$

$$Ni^{2+} + 2OH^- \rightarrow Ni(OH)_{2(s)} \quad (5)$$

According to the Schikorr reaction, ferrous hydroxide can be an intermediate between elementary iron and magnetite [51]:

$$3Fe(OH)_{2(s)} \rightarrow Fe_3O_{4(s)} + 2H_2O + H_{2(g)} \quad (6)$$

Indeed, magnetite is a typical secondary phase frequently detected for steel corroded under HLRW repository-relevant conditions [23–25,52]. An alternative possibility would be the solid-state transport of charge carriers in the compact passivation layer, with water reduction occurring at the corrosion layer/brine interface [53].

On the surface, $Fe(OH)_2$ can also be dehydrated to form Fe oxides, and $Ni(OH)_2$ may undergo comparable reaction, following [50]:

$$Fe(OH)_{2(s)} \rightarrow FeO_{(s)} + H_2O \quad (7)$$

$$2Fe(OH)_{2(s)} \rightarrow Fe_2O_{3(s)} + H_2O + H_{2(g)} \quad (8)$$

$$Ni(OH)_{2(s)} \rightarrow NiO_{(s)} + H_2O \quad (9)$$

According to these equations, the passive film would be composed of an inner Cr-rich layer and an outer Fe- and Ni-rich layer. In the outer-layer, various Fe oxides may prevail simultaneously (Eqs. (6–8)). Because Fe and Ni have very comparable sizes, $Ni^{2+}$ may substitute for $Fe^{2+}$ in ferrous hydroxide, resulting in the formation of Ni-doped magnetite. Likewise, $Fe^{2+}$ can substitute for $Ni^{2+}$ in $Ni(OH)_2$ and form Fe-doped NiO.

Because of the lower diffusion rate of Cr compared to Fe and Ni in the oxide film and due to the inward diffusion of $OH^-$, $Fe^{2+}$ and $Ni^{2+}$ ions can also react with $Cr_2O_3$ in the inner-layer to form chromite-nichromite (i.e., Ni-containing chromite) compounds [49]:

$$xNi^{2+} + (1-x)\,Fe^{2+} + Cr_2O_{3(s)} + 2OH^- \rightarrow \left(Ni_xFe_{1-x}\right)Cr_2O_{4(s)} + H_2O \quad (10)$$

However, the lower Ni and higher Fe content in 309 S make it more likely to form Fe chromite species rather than Ni chromite. By analogy with the previous reaction, it is reasonable to assume that $Ni^{2+}$ can react with $Fe_2O_3$ present in the outer layer to form trevorite [49]:

$$Ni^{2+} + Fe_2O_{3(s)} + 2OH^- \rightarrow NiFe_2O_{4(s)} + H_2O \quad (11)$$

Based on these equations, the oxide film covering the corroding steel surface would be composed of a Cr-rich inner-layer made of $Cr_2O_3$ and $Ni_xFe_{(1-x)}Cr_2O_4$ and an outer-layer rich in Fe and Ni oxides such as magnetite, trevorite and NiO. This description of the oxide film forming on stainless steel agrees with usually reported compositions of passive films formed on austenitic stainless steels [49,54,55]. All compounds mentioned in equation reactions above have been detected in the microspectroscopic analyses. Because of very similar backscattering properties, it is very likely that formed spinels are not pure but contain trace amounts of substituting elements (e.g., $Ni^{2+}$ substituting for $Fe^{2+}$ and $Cr^{3+}$ substituting for $Fe^{3+}$).

Several reactions suggest the consumption of hydroxide ions counterbalancing their formation by water reduction. The resulting absence of significant pH variation agrees with experimental results (Fig. 2). Water reduction results in the formation of hydrogen (Reaction (2)), which may also be produced according to Reactions (6) and (8), implying an expected development of reducing conditions. The absence of significant $E_h$ decrease during experiments may suggest that $H_{2(g)}$ did not accumulate within reactors but rather escaped, which would agree with the absence of observed pressure build-up. Note however that redox electrodes require the presence of a certain concentration of reactive redox species in order to display reliable $E_h$ values. The relatively high $E_h$ value can be explained by the low corrosion extent, visible by the low concentrations of Fe(II) and $H_{2(g)}$.

It is also worth noting that no pit could be observed at the surface of any corroded coupon, either because their formation was not initiated owing to good protection of the surface by the passivation layer, because they were too small to be observed or because of their scarcity. Corrosion experiments using the same steel and brines under anoxic and elevated temperature (90 °C) conditions, but under flowing conditions (60 mL/day), have been reported [56]. The analysis by 3D-interferometry of the surface of coupons corroded for 160 days revealed a very low corrosion damage with scarce formation of small pits (< 2 μm deep) and no significant surface roughness developed. The reported absence of significant change of surface roughness agrees with results of the present study. The detection of more subtle evolution of the surface morphology in the present study would have required the application of light interferometry, which is able to detect minute height differences on the surface [57].

**Table 8**
Half-reaction of Cr, Fe and Ni reduction with the associated potential.

| Half-reaction | Potential (V vs S.H.E., 25 °C) | Source |
|---|---|---|
| $Ni^{2+} + 2\,e^- \Leftrightarrow Ni_{(cr)}$ | − 0.237 | [67] |
| $Fe^{2+} + 2\,e^- \Leftrightarrow Fe_{(cr)}$ | − 0.440 | [68] |
| $Cr^{3+} + 3\,e^- \Leftrightarrow Cr_{(cr)}$ | − 0.677 | [44] |

### 4.2. Effect of temperature

Increasing the temperature shifts the corrosion potential of stainless steel to lower values and decreases the protection properties of the film [49]. The amounts of Fe and Ni dissolved from the metallic surface increase and their diffusion in the corrosion layer increases their concentration within the film, especially in the outer-layer. In turn, the film thickness may increase with time and possibly affect the solid-state transport of charge carriers within the compact film. The composition of the corrosion layer may thus depend on both the diffusion properties of charge carriers within the film and the solubility in the contacting brine of the elements constitutive of the film. It is also very likely that these processes may be affected by the high chloride content of the contacting brines.

At elevated temperatures and in low saline conditions, reported Pourbaix diagrams for the ternary Fe-Cr-Ni system revealed a complicated interplay of reactions, sometimes involving several metal oxides [58]. Among them spinels play an important role because of their very low solubility. Bimetallic spinel oxides such as chromite ($FeCr_2O_4$) and trevorite ($NiFe_2O_4$) have large stability fields and are more stable than magnetite. Among iron species trevorite has the largest stability area, existing in a wide potential range, but becomes less stable than $\alpha$-$Fe_2O_3$ for decreasing pH values (pH $<$ ~6.5) and less stable than chromite at lower potentials ($E_h$ $<$ ~0 mV). Trevorite is also the most stable Ni species expected to form under the applied geochemical conditions. Chromite and $Cr_2O_3$ are the most stable chromium species under relevant potential/pH conditions at 90 °C, together with $Cr(OH)_3$ at lower Cr concentrations. Because the steel is made of three main elements, more than one solid phase can be formed at a given potential/pH condition [58], which is indeed corroborated by experimental findings of this study.

### 4.3. Composition of the brine and nature of corrosion products

The identified corrosion products are mostly low soluble oxide compounds, and despite the high chloride content, no presence of Cl-bearing phase other than CrFeNi-LDH could be detected. The presence of e.g., ferrous hydroxychloride has been evidenced in the corrosion layer of archeological artefacts [59,60] and in in situ steel corrosion experiments in contact with clay borehole water [25,26]. Yet, the chloride content is high in the present study, especially in $MgCl_2$ brine, but the amounts of dissolved ferrous ions are very low (Table 3). The absence of ferrous hydroxychloride may thus suggest that the prevailing geochemical conditions (e.g., low amounts of dissolved ferrous ions) were unfavorable to the formation of such compound or that the corrosion is efficiently inhibited by the passivation layer. Because the composition of the corrosion layer for the coupon exposed to $MgCl_2$ could not be determined as in the case of the coupon exposed to NaCl, no direct connection between nature of formed corrosion products and brine composition could be established. However, the substitution of $Fe^{2+}$ or $Ni^{2+}$ by $Mg^{2+}$ may occur in the $MgCl_2$ brine because of comparable sizes [61].

### 4.4. Implications for nuclear waste disposal in high saline environments

The good resistance to general corrosion compares well with reported findings for in situ experiments performed at comparable temperature but for longer contact times [21]. However, a low tendency to local corrosion was detected in field experiments but not in the present study. This difference between field and laboratory experiments may be attributed to the time needed for pits to develop under the applied conditions, possibly to the presence of additional cationic or anionic species (e.g., $K^+$, $Ca^{2+}$, $SO_4^{2-}$) in the contacting brine in the salt rock, or to mechanical damages of the passivation layer by contact with solid material.

According to current concepts of HLRW disposal sites (e.g., [2]), groundwater may reach the primary stainless steel containers only after failure of the overpack. By that time, the temperature at the surface of the containers will have further decreased and near-field conditions may have evolved compared to that prevailing when the overpack starts corroding. For clay-based repositories, reactive transport modelling suggests that the pH at the corroding container/bentonite interface may increase by several units within several thousands of years [62–64]. For a repository hosted in salt rock, a comparable or even more significant pH evolution may be anticipated because e.g., crushed salt used as backfill has a lower pH buffer capacity than bentonite or argillite. Rather accessory minerals such as e.g., saltclay or the impact of sealing and backfill materials (e.g., Sorel phases and salt concrete) will determine solution pH. In order to limit pH decrease, MgO can be used as additive to backfill material, this strategy has been proposed for the Waste Isolation Pilot Plant (USA) for buffering $CO_2$ evolution from organic waste constituents [65]. In alkaline environments, stainless steels are relatively resistant to general corrosion [21], with the formation of a bi-layer of corrosion products made of low soluble compounds, as evidenced in the present study.

However, results of experiments performed in the laboratory with polished samples should be transferred carefully to real container surfaces, which may be rougher and have scratches, resulting in a different reactivity. Another aspect to bear in mind is the amount of available water, which is expected to be relatively limited in salt rock. Solutions might be present because of seepage resulting from incomplete repository backfilling or because of the presence of non-detected brine pockets. The presence of water in significant amounts can be considered highly unlikely, but is considered within so called "what-if" cases in order to assess the robustness of a repository concept. With limited water available, corrosion rates would be lower than that obtained in the present study by suspending coupons in brines. Still, one has to assume that even at low corrosion rates, after sufficient time (thousands of years) stainless steel containers will corrode as long as access of aqueous solutions is available. The current study indicates that various corrosion phases will then form. It is, however, not yet clear how formation, dissolution and transport rates (e.g. by diffusion) determine relevant secondary phase layers coming into contact with radionuclides dissolving from the vitrified waste. It is likely that thermodynamically stable and low solubility mineral phases such as Cr/Ni/Fe-oxides/hydroxides (such as bimetallic spinel compounds for instance) will persist and form a layer, which might represent a first barrier for radionuclides. Projection to longer contact times to identify possibly persisting phases may be provided by reactive transport modeling, as it has been done for systems representative of clay-based disposal sites [62–64,66]. However, this would require a Pitzer database to be available for calculating activity coefficients of dissolved species present in highly saline aqueous solutions, which is not yet the case.

## 5. Conclusion

An austenitic stainless steel was exposed to concentrated salt brines at 90 °C under anoxic conditions and corroded samples were analyzed by complementary microscopic and spatially resolved spectroscopic techniques. The surface damage was limited after 294 days of contact time and no local surface attack could be detected. The preparation of cross-sections allowed identifying the formation of a thin corrosion layer ($\leq$ 1 μm). The layer has a duplex structure consisting of a Cr-rich inner layer and a Fe- and Ni-rich outer layer, which compares well with reported findings on stainless steels. The inner layer is mostly made of $Cr_2O_3$ and Cr-rich spinel type compounds, the outer layer is constituted by magnetite and trevorite, both doped with low amounts of Cr, and admixed NiO and $Ni(OH)_2$. It can be hypothesized that in the early stages the surface was first passivated by $Cr_2O_3$ and $Cr(OH)_3$. With increasing contact time, Fe and Ni dissolved from the surface and migrated

through pores and defects within the film, resulting in the formation of hydroxides in contact with the brine, which then converted into oxides. The limited surface attack and the formation of low soluble compounds correlate well with the limited evolution of pH, $E_h$ and dissolved amounts of metal ions for experiments performed in NaCl brines. The surface attack was lower in $MgCl_2$ brines and the observed pH and $E_h$ evolutions were within uncertainties.

The main outcomes suggest a good resistance to general corrosion under the applied conditions, which agrees with earlier field studies performed at 90 °C for over 10 years in a former salt mine. However, no pit formation could be detected on any sample with the analytical techniques used in the present study. pH and $E_h$ progressively evolved with time in experiments performed in NaCl brines without reaching a constant value. This is likely due to low corrosion rates and low concentrations of dissolved redox pairs. Longer contact times may also be needed to reach the onset for corrosion in concentrated $MgCl_2$ brines.

## Author statement

The authors declare that the science contained in this manuscript has not been previously published and is not under consideration by any other journal.

## CRediT authorship contribution statement

N.F.: Conceptualization, funding acquisition, supervision, formal analysis, writing-original draft, review and editing; N.M.: Conceptualization, sample preparation, formal analysis, writing-review and editing; M.L.S: Formal analysis, writing-review and editing; D.S.: Formal analysis, writing-review and editing; S.R.: Formal analysis, writing-review and editing; K.D.: writing-review and editing; H.G.: supervision, writing-review and editing.

## Declaration of Competing Interest

The authors declare that they have no known competing financial interests or personal relationships that could have appeared to influence the work reported in this paper.

## Data Availability

The raw/processed data required to reproduce these findings will be shared by the corresponding author upon reasonable request.

## Acknowledgements

We acknowledge the SOLEIL synchrotron and the KIT Light Source for the provision of synchrotron radiation beamtime. We would like to thank the Institute for Beam Physics and Technology (IBPT) for the operation of the storage ring, the Karlsruhe Research Accelerator (KARA). We also acknowledge the workshop of KIT-INE for the construction of the setups. Stephanie Kraft (KIT-INE, Germany) is gratefully acknowledged for AFM measurements and Dr. Ruth Haas-Nüesch (KIT-AGW, Germany) for providing the chromite reference compound. This work has received funding from the German Federal Ministry of Economic Affairs and Energy (BMWi) under grant agreement no. 02 E 11496 B (KORSO project).

## Appendix A. Supporting information

Supplementary data associated with this article can be found in the online version at doi:10.1016/j.corsci.2023.111265.

## References

[1] F. Cattant, D. Crusset, D. Feron, Corrosion issues in nuclear industry today, Mater. Today 11 (2008) 32–37.
[2] D. Feron, D. Crusset, J.M. Gras, Corrosion issues in nuclear waste disposal, J. Nucl. Mater. 379 (2008) 16–23.
[3] Endlagerkommission, Abschlussbericht der Kommission Lagerung hoch radioaktiver Abfallstoffe, K-Drs. 268, in, Berlin, Germany, 2016, pp. 1–681.
[4] W. Brewitz, Zusammenfassender Zwischenbericht, GSF T 114, in, 1980.
[5] NWMO, Postclosure Safety Assessment of a Used Fuel Repository in Sedimentary Rock, Report NWMO-TR-2018–08, in, NWMO, Toronto, Canada, 2018, pp. 1–704.
[6] G. George, H. Shaikh, 1 - Introduction to austenitic stainless steels, in: H.S. Khatak, B. Raj (Eds.), Corrosion of Austenitic Stainless Steels, Woodhead Publishing, 2002, pp. 1–36.
[7] D.G. Bennett, R. Gens, Overview of European concepts for high-level waste and spent fuel disposal with special reference waste container corrosion, J. Nucl. Mater. 379 (2008) 1–8.
[8] NAGRA, Project Opalinus Clay, Safety Report, Demonstration of disposal feasibility for spent fuel, vitrified high-level waste and long-lived intermediate-level waste (Entsorgungsnachweis), NTB 02–05, in, NAGRA, Wettingen, Switzerland, 2002, pp. 1–472.
[9] E. McCafferty, Introduction to corrosion science, 2010.
[10] U.K. Mudali, M.G. Pujar, 3 - Pitting corrosion of austenitic stainless steels and their weldments, in: H.S. Khatak, B. Raj (Eds.), Corrosion of Austenitic Stainless Steels, Woodhead Publishing, 2002, pp. 74–105.
[11] F. King, Container materials for the storage and disposal of nuclear waste, Corrosion 69 (2013) 986–1011.
[12] E.C. Gaucher, C. Tournassat, F.J. Pearson, P. Blanc, C. Crouzet, C. Lerouge, S. Altmann, A robust model for pore-water chemistry of clayrock, Geochim. Cosmochim. Acta 73 (2009) 6470–6487.
[13] Pearson, F.J., D. Arcos, A. Bath, J.-Y. Boisson, A.M. Fernández, H.-E. Gäbler, E.C. Gaucher, A. Gautschi, L. Griffault, P. Hernán, H.N. Waber, Mont Terri Project – Geochemistry of Water in the Opalinus Clay Formation at the Mont Terri Rock Laboratory, in: F. Federal Office for Water and Geology (Ed.) Reports of the FOWG, Geology Series No. 5, Bern-Ittigen, 2003, pp. 1–321.
[14] F. King, D.S. Hall, P.G. Keech, Nature of the near-field environment in a deep geological repository and the implications for the corrosion behaviour of the container, in: Corrosion Engineering Science and Technology, 52, 2017, pp. 25–30.
[15] B. Kienzler, A. Loida, Endlagerrelevante Eigenschaften von hochradioaktiven Abfallprodukten. Charakterisierung und Bewertung. Empfehlung des Arbeitskreises HAW-Produkte, Forschungszentrum Karlsruhe, Karlsruhe, 2001, pp. 1–118.
[16] J.F. Lucchini, M. Borkowski, M.K. Richmann, S. Ballard, D.T. Reed, Solubility of $Nd^{3+}$ and $UO_2^{2+}$ in WIPP brine as oxidation-state invariant analogs for plutonium, J. Alloy. Compd. 444–445 (2007) 506–511.
[17] J.A. Schramke, E.F.U. Santillan, R.T. Peake, Plutonium oxidation states in the Waste Isolation Pilot Plant repository, Appl. Geochem. 116 (2020) 104561.
[18] SKB, Long-term safety for the final repository for spent nuclear fuel at Forsmark. Main report of the SR-Site project. Volume I., in, Svensk Kärnbränslehantering AB, Stockholm, 2015, pp. 276.
[19] P. Oy, Safety Case for the Disposal of Spent Nuclear Fuel at Olkiluoto – Complementary Considerations 2012, in, Posiva Oy, Eurajoki,Finland, 2012, pp. 262.
[20] H.P. Leckie, H.H. Uhlig, Environmental factors affecting the critical potential for pitting in 18–8 stainless steel, J. Electrochem. Soc. 113 (1966) 1262.
[21] B. Kursten, E. Smailos, I. Azkarate, L. Werme, N.R. Smart, G. Santarini, State-of-the-art document on the COrrosion BEhaviour of COntainer, MAterials, (2004) 1–299.
[22] J.H. Johnson, M. Niemeyer, G. Klubertanz, P. Siegel, P. Gribi, Calculations of the Temperature Evolution of a Repository for Spent Fuel, Vitrified High-Level Waste and Intermediate Level Waste in Opalinus Clay, NTB 01–04, in, NAGRA, Wettingen, Switzerland, 2002, pp. 1–80.
[23] B. Reddy, C. Padovani, A.P. Rance, N.R. Smart, A. Cook, H.M. Haynes, A.E. Milodowski, L.P. Field, S.J. Kemp, A. Martin, N. Diomidis, The anaerobic corrosion of candidate disposal canister materials in compacted bentonite exposed to natural granitic porewater containing native microbial populations, Mater. Corros. Werkst. Korros. 72 (2021) 361–382.
[24] N.R. Smart, B. Reddy, A.P. Rance, D.J. Nixon, M. Frutschi, R. Bernier-Latmani, N. Diomidis, The anaerobic corrosion of carbon steel in compacted bentonite exposed to natural Opalinus Clay porewater containing native microbial populations, Corros. Eng. Sci. Technol. 52 (2017) 101–112.
[25] M.L. Schlegel, S. Necib, S. Daumas, C. Blanc, E. Foy, N. Trcera, A. Romaine, Microstructural characterization of carbon steel corrosion in clay borehole water under anoxic and transient acidic conditions, Corros. Sci. 109 (2016) 126–144.
[26] S. Necib, Y. Linard, D. Crusset, N. Michau, S. Daumas, E. Burger, A. Romaine, M.L. Schlegel, Corrosion at the carbon steel-clay borehole water and gas interfaces at 85 degrees C under anoxic and transient acidic conditions, Corros. Sci. 111 (2016) 242–258.
[27] E. Smailos, B. Fiehn, In-situ Corrosion Testing of Selected HLW Container Materials under the Conditions of the HLW Test Disposal in the Asse Salt Mine, Forschungszentrum Karlsruhe, Karlsruhe, 1995, pp. 1–23.
[28] A. Gaudin, D. Bartier, L. Truche, E. Tinseau, F. Foct, V. Dyja, A. Maillet, D. Beaufort, First corrosion stages in Tournemire claystone/steel interaction: In situ experiment and modelling approach, Appl. Clay Sci. 83–84 (2013) 457–468.
[29] A. Gaudin, S. Gaboreau, E. Tinseau, D. Bartier, S. Petit, O. Grauby, F. Foct, D. Beaufort, Mineralogical reactions in the Tournemire argillite after in-situ

interaction with steels, Appl. Clay Sci. 43 (2009) 196–207.
[30] S. Necib, M.L. Schlegel, C. Bataillon, S. Daumas, N. Diomidis, P. Keech, D. Crusset, Long-term corrosion behaviour of carbon steel and stainless steel in Opalinus clay: influence of stepwise temperature increase, Corros. Eng. Sci. Technol. 54 (2019) 516–528.
[31] M. Altmaier, V. Metz, V. Neck, R. Muller, T. Fanghanel, Solid-liquid equilibria of $Mg(OH)_2$(cr) and $Mg_2(OH)_3Cl{\cdot}4H_2O$(cr) in the system Mg-Na-H-OH-O-Cl-$H_2O$ at 25°C, Geochim. Cosmochim. Acta 67 (2003) 3595–3601.
[32] D.L. Parkhurst, C.A.J. Appelo, User's guide to PHREEQC (Version 2): A computer program for speciation, batch-reaction, one-dimensional transport, and inverse geochemical calculations, in: Water-Resources Investigations Report, 1999.
[33] M. Grive, L. Duro, E. Colas, E. Giffaut, Thermodynamic data selection applied to radionuclides and chemotoxic elements: An overview of the ThermoChimie-TDB, Appl. Geochem. 55 (2015) 85–94.
[34] L. Ciavatta, The specific interaction theory in evaluating ionic equilibria, Ann. Chim. 70 (1980) 551–567.
[35] P.H. Barry, JPCALC, A software package for calculating liquid-junction potential corrections in patch-clamp, intracellular, epithelial and bilayer measurements and for correcting junction potential measurements, J. Neurosci. Methods 51 (1994) 107–116.
[36] M.P. Seah, L.S. Gilmore, G. Beamson, XPS: Binding energy calibration of electron spectrometers 5 - Re-evaluation of the reference energies, Surf. Interface Anal. 26 (1998) 642–649.
[37] NIST, X-ray Photoelectron Spectroscopy Database, Version 4.1, in, National Institute of Standards and Technology, Gaithersburg, 2012, pp. ⟨https://srdata.nist.gov/xps/⟩.
[38] S. Reguer, C. Mocuta, D. Thiaudiere, M. Daudon, D. Bazin, Combination of X-ray synchrotron radiation techniques to gather information for clinicians, Comptes Rendus Chim. 19 (2016) 1424–1431.
[39] V.A. Sole, E. Papillon, M. Cotte, P. Walter, J. Susini, A multiplatform code for the analysis of energy-dispersive X-ray fluorescence spectra, Spectrochim. Acta Part B At. Spectrosc. 62 (2007) 63–68.
[40] A. Dawiec, Y. Garreau, J. Bisou, S. Hustache, B. Kanoute, F. Picca, G. Renaud, A. Coati, Real-time control of the beam attenuation with XPAD hybrid pixel detector, J. Instrum. 11 (2016) P12018.
[41] B. Ravel, M. Newville, ATHENA, ARTEMIS, HEPHAESTUS: data analysis for X-ray absorption spectroscopy using IFEFFIT, J. Synchrotron Radiat. 12 (2005) 537–541.
[42] J. Rothe, S. Butorin, K. Dardenne, M.A. Denecke, B. Kienzler, M. Loble, V. Metz, A. Seibert, M. Steppert, T. Vitova, C. Walther, H. Geckeis, The INE-Beamline for actinide science at ANKA, Rev. Sci. Instrum. 83 (2012).
[43] D.R. Lide, CRC Handbook of Chemistry and Physics, 85th edition., Taylor & Francis, 2004.
[44] J. Chivot, Thermodynamique des produits de corrosion. Fonctions thermodynamiques, diagrammes de solubilité, diagrammes E-pH des systèmes Fe-$H_2O$, Fe-$CO_2$-$H_2O$, Fe-S-$H_2O$, Cr-$H_2O$ et Ni-$H_2O$ en fonction de la température., ANDRA, Châtenay-Malabry, France, 2004.
[45] S. Venugopal, S.L. Mannan, Y. Prasad, Influence of strain rate and state-of-stress on the formation of ferrite in stainless steel type AISI 304 during hot working, Mater. Lett. 26 (1996) 161–165.
[46] D. Garai, V. Solokha, A. Wilson, I. Carlomagno, A. Gupta, M. Gupta, V.R. Reddy, C. Meneghini, F. Carla, C. Morawe, J. Zegenhagen, Studying the onset of galvanic steel corrosion in situ using thin films: film preparation, characterization and application to pitting, J. Phys. Condens. Matter 33 (2021) 125001.
[47] M.C. Biesinger, B.P. Payne, A.P. Grosvenor, L.W.M. Lau, A.R. Gerson, R.S. Smart, Resolving surface chemical states in XPS analysis of first row transition metals, oxides and hydroxides: Cr, Mn, Fe, Co and Ni, Appl. Surf. Sci. 257 (2011) 2717–2730.
[48] S.E. Ziemniak, M.E. Jones, K.E.S. Combs, Solubility and phase behavior of Cr(III) oxides in alkaline media at elevated temperatures, J. Solut. Chem. 27 (1998) 33–66.
[49] Z.G. Duan, F. Arjmand, L.F. Zhang, H. Abe, Investigation of the corrosion behavior of 304L and 316L stainless steels at high-temperature borated and lithiated water, J. Nucl. Sci. Technol. 53 (2016) 1435–1446.
[50] H.T. Zeng, Y. Yang, M.H. Zeng, M.C. Li, Effect of dissolved oxygen on electrochemical corrosion behavior of 2205 duplex stainless steel in hot concentrated seawater, J. Mater. Sci. Technol. 66 (2021) 177–185.
[51] G. Schikorr, Über Eisen(II)-hydroxyd und ein ferromagnetisches Eisen(III)-hydroxyd, Z. Anorg. Allg. Chem. 212 (1933) 33–39.
[52] M.L. Schlegel, C. Bataillon, K. Benhamida, C. Blanc, D. Menut, J.L. Lacour, Metal corrosion and argillite transformation at the water-saturated, high-temperature iron-clay interface: A microscopic-scale study, Appl. Geochem. 23 (2008) 2619–2633.
[53] C. Bataillon, F. Bouchon, C. Chainais-Hillairet, C. Desgranges, E. Hoarau, F. Martin, S. Perrin, M. Tupin, J. Talandier, Corrosion modelling of iron based alloy in nuclear waste repository, Electrochim. Acta 55 (2010) 4451–4467.
[54] V. Maurice, W.P. Yang, P. Marcus, X-ray photoelectron spectroscopy and scanning tunneling microscopy study of passive films formed on (100) Fe-18Cr-13Ni single-crystal surfaces, J. Electrochem. Soc. 145 (1998) 909–920.
[55] B. Stellwag, The mechanism of oxide film formation on austenitic stainless steels in high temperature water, Corros. Sci. 40 (1998) 337–370.
[56] C. Sisk-Scott, C. Marrs, Graphite Steel and Chromium-Nickel Steel Corrosion: Solution Flow-Through Corrosion Experiments. Report SAND2019–13627R, Sandia National Laboratories, Carlsbad, New Mexico, USA, 2019.
[57] E.Q. Contreras, J. Huang, R.S. Posusta, D.K. Sharma, C. Yan, P. Guraieb, M.B. Tomson, R.C. Tomson, Optical measurement of uniform and localized corrosion of C1018, SS 410, and Inconel 825 alloys using white light interferometry, Corros. Sci. 87 (2014) 383–391.
[58] B. Beverskog, I. Puigdomenech, Pourbaix diagrams for the ternary system of iron-chromium-nickel, Corrosion 55 (1999) 1077–1087.
[59] S. Reguer, P. Dillmann, F. Mirambet, Buried iron archaeological artefacts: Corrosion mechanisms related to the presence of Cl-containing phases, Corros. Sci. 49 (2007) 2726–2744.
[60] C. Remazeilles, D. Neff, F. Kergourlay, E. Foy, E. Conforto, E. Guilminot, S. Reguer, P. Refait, P. Dillmann, Mechanisms of long-term anaerobic corrosion of iron archaeological artefacts in seawater, Corros. Sci. 51 (2009) 2932–2941.
[61] R.D. Shannon, Revised effective ionic radii and systematic studies of interatomic distances in halides and chalcogenides, Acta Crystallogr. Sect. A 32 (1976) 751–767.
[62] O. Bildstein, L. Trotignon, M. Perronnet, M. Jullien, Modelling iron-clay interactions in deep geological disposal conditions, Phys. Chem. Earth 31 (2006) 618–625.
[63] M.C. Chaparro, N. Finck, V. Metz, H. Geckeis, Reactive transport modelling of the long-term interaction between carbon steel and MX-80 bentonite at 25 degrees C, Minerals 11 (2021) 1272.
[64] J. Samper, A. Naves, L. Montenegro, A. Mon, Reactive transport modelling of the long-term interactions of corrosion products and compacted bentonite in a HLW repository in granite: Uncertainties and relevance for performance assessment, Appl. Geochem. 67 (2016) 42–51.
[65] V. Monastra, D.E. Grandstaff, Kinetics of MgO dissolution and buffering of fluids in the Waste Isolation Pilot Plant (WIPP) repository, in: Materials Research Society Symposium - Proceedings, 1999, pp. 625–632.
[66] J.C. Wilson, S. Benbow, H. Sasamoto, D. Savage, C. Watson, Thermodynamic and fully-coupled reactive transport models of a steel-bentonite interface, Appl. Geochem. 61 (2015) 10–28.
[67] H. Gamsjäger, J. Bugajski, T. Gajda, R.J. Lemire, W. Preis, Chemical Thermodynamics of Nickel, North Holland Elsevier Science Publishers B. V., Amsterdam, The Netherlands, 2005.
[68] R.J. Lemire, U. Berner, C. Musikas, D.A. Palmer, P. Taylor, O. Tochiyama, Chemical thermodynamics of iron - Part 1, OECD Nuclear Energy Agency Data Bank ed., Issy-les-Moulineaux, France, 2013.